Millimeter-Level Pick and Peg-in-Hole Task Achieved by Aerial Manipulator

Meng Wang, Zeshuai Chen, Kexin Guo, Xiang Yu, Youmin Zhang, *Fellow, IEEE*, Lei Guo, *Fellow, IEEE*, and Wei Wang

***Abstract*—Achieving accurate control performance of the end-effector is critical for practical applications of aerial manipulator. However, due to the presence of floating-base disturbance from the unmanned aerial vehicle (UAV) platform and the kinematic error amplification effect from multilink structure of the manipulator, it is extremely challenging to ensure the high-precision performance of aerial manipulator. Building upon the philosophy of disturbance rejection, we propose a predictive optimization scheme that allows aerial manipulator to successfully execute millimeter-level flying pick and peg-in-hole task. First, the error amplification effect of the floating base is quantitatively analyzed by virtue of the aerial manipulator kinematics. Intuitively, it is found that if the further motion of the UAV platform is well predicted, the manipulator can directly counteract the floating disturbance by following a modified reference trajectory. Hence, a learning-based prediction approach is leveraged to rapidly forecast the UAV platform motion online. Subsequently, an optimization controller is formulated to follow the reference trajectory by incorporating multiple practical constraints of aerial manipulator. Flight tests demonstrate that this study goes a step further to achieve higher accuracy of the end-effector than the existing results (centimeter-level).**

***Index Terms*—Disturbance rejection, floating-base disturbance, kinematic error amplification, multiple constraints, predictive optimization scheme.**

Manuscript received 7 August 2023; accepted 14 November 2023. Date of publication 4 December 2023; date of current version 8 January 2024. This paper was recommended for publication by Associate Editor G. Heredia and Editor P. Robuffo Giordano upon evaluation of the reviewers' comments. This work was supported in part by the Defense Industrial Technology Development Program under Grant JCKY2020601C016, in part by the National Natural Science Foundation of China under Grant 61833013, Grant 61973012, Grant 62388101, and Grant 62273023, in part by the National Key Research and Development Program of China under Grant 2022YFB4701301, in part by the Key Research and Development Program of Zhejiang under Grant 2021C03158, in part by the Major Science and Technology Innovation Program of Hangzhou under Grant 2022AIZD0137, and in part by the Beijing Nova Program under Grant 20230484266. *(Corresponding author: Xiang Yu.)*

Meng Wang, Zeshuai Chen, Xiang Yu, and Lei Guo are with the School of Automation Science and Electrical Engineering, Beihang University, Beijing 100191, China (e-mail: mwangbuaa@126.com; zschenbuaa@126.com; xiangyu_buaa@buaa.edu.cn; lguo@buaa.edu.cn).

Kexin Guo is with the School of Aeronautical Science and Engineering, Beihang University, Beijing 100191, China (e-mail: kxguo@buaa.edu.cn).

Youmin Zhang is with the Department of Mechanical, Industrial and Aerospace Engineering, Concordia University, Montreal, QC H3G 1M8, Canada (e-mail: ymzhang@encs.concordia.ca).

Wei Wang is with the China Aerospace Science and Technology Corporation, Beijing 100048, China, and also with the Beijing Institute of Aerospace Control Devices, Beijing 100039, China (e-mail: yfwangwei@vip.sina.com).

This article has supplementary downloadable material available at https://doi.org/10.1109/TRO.2023.3338956, provided by the authors.

Digital Object Identifier 10.1109/TRO.2023.3338956

I. Introduction

Aerial manipulator, composed of a robot-wing unmanned aerial vehicle (UAV) and a multilink manipulator, has received considerable attention in recent years [1], [2], [3]. The active feature of aerial manipulator propels applications into more complicated interactive scenarios. It is not a far stretch that aerial manipulator is applied to remove obstacles on high-voltage power lines, transport components to a narrow area, and restore infrastructure facilities.

It is obvious that applications of aerial manipulators are highly dependent on the precise control performance of the end-effector. However, different from traditional fixed-base robotic systems, the base of aerial manipulator is fluctuated resulting from multiple disturbances. First of all, the control accuracy of the UAV platform is significantly degraded in the presence of model uncertainties. The extra dynamic coupling disturbances caused by the operating manipulator also aggravate the UAV fluctuation. In addition, due to the presence of the error amplification as shown in Section III-C, even slight fluctuation of the UAV platform can substantially increase the sway of the end-effector, tremendously deteriorating the control performance. It is evidently seen that the unmodeled and nonlinear floating-base disturbance is one of the most notable challenges to precise end-effector control. Enticed by expansive potential applications of aerial manipulators, plenty of studies are presented from different views to attain the high-precision performance of the end-effector, such as structure design [4], [5], [6], [7], [8], [9], [10], [11], [12], [13], precise aerial platform control [14], [15], [16], [17], [18], [19], [20], [21], [22], and precise manipulator control [23], [24], [25], [26], [27], [28], just to mention a few.

A common approach to enhance the accuracy of the end-effector is the use of new mechanisms. The parallel delta-type arm structure intends to improve the control accuracy. However, its operating workspace is greatly limited to the constrained area underneath the UAV platform. Meanwhile, advanced control techniques are developed to improve control performance of the end-effector [14], [15], [16], [17], [18], [19], [20], [21], [22], [23], [24], [25], [26], [29]. Nonetheless, it is difficult to fully handle the floating-base disturbance, which substantially impedes the tracking performance of aerial manipulator. Hence, the accuracy of the end-effector is mostly ensured in the centimeter level currently [15], [16], [19], [25], [30]. Unlike existing concept of designing dynamic controllers, one alternative solution for tackling the floating-base disturbance is to utilize the capability of the manipulator. With the recomputed manipulator joint signals, it may reduce the effect of the floating-base disturbance on the tracking performance of the end-effector at the cost of complex iterative inverse kinematic algorithm [5], [25]. In the case that the moving base is a massive inertial platform, the mobile manipulator control problem is formulated in [26], [27], [28]. Nevertheless, the strict assumption that the operation of manipulator cannot affect the platform motion must be held. To meet the intractable constraint, the inertia of the UAV platform must be significantly larger than that of the manipulator. In addition, the control input signal may be discontinuous and abrupt [26], even resulting in the undesired protection stop of the low-level dynamic controller of manipulator.

Driven by the aforementioned analysis, we focus on the design of a control scheme to enable the high-precision control of the end-effector. More specially, on the basis of disturbance rejection philosophy, a learning-based predictive optimization scheme is proposed to achieve millimeter-level position-error tracking performance. To recap, the contributions of this article are summarized as follows.

1) As compared to compensation or attenuation methods [15], [19], [23], [24], [25], a disturbance rejection approach is developed to handle the floating-base disturbance. The kinematic relationship is exploited to replan the desired trajectory of manipulator in the base frame $\mathcal{F}_\Delta$ to dissolve the UAV fluctuation. This means that the system does not require aggressive control commands to compensate for disturbances. In addition, in contrast to the previous work [26], [27], a learning-based prediction approach is employed to rapidly forecast the UAV platform motion online, despite unknown external disturbances and varying dynamic process. The proposed learning-based prediction method can decouple the relationship between the manipulator and the platform, reducing the control conservativeness.
2) By virtue of motion prediction information, an optimization control strategy is proposed to achieve millimeter-level control accuracy of the end-effector. When comparing to the existing studies [26], [27], [28], the acceleration of the end-effector is intuitively considered as the control sequence in the task space to maximize smoothness of control action. Besides, in comparison to the fixed-base robots, the effective workspace of the end-effector is restricted to the underside of the propellers and the inner side of the UAV outer frame. Therefore, to ensure safety, multiple practical constraints of aerial manipulator are incorporated in the controller design, including kinematic feasibility, actuators limitation, and dynamical constraint.

A set of experiments has demonstrated that the proposed scheme outperforms existing studies. Compared with feedback-based controller [23] and potential field-based controller [24], an average improvement of over 70% and 50% using the proposed scheme in real flight tests has been achieved. Moreover, experiment II and experiment III illustrate the robustness to unknown disturbances and online adaptive ability for varying dynamic process. Furthermore, a challenging pick and peg-in-hole task is accomplished. The aerial manipulator can pick up a pen with a diameter of 11 mm, and subsequently insert the pen precisely into a narrow hole with a diameter of 20 mm. To the best of the authors' knowledge, this is currently the highest accuracy in the pick and peg-in-hole task using aerial manipulator.

The rest of this article is arranged as follows. Related work for improving the accuracy of the end-effector is depicted in Section II. Some comprehensive problem analyses are expounded in Section III. Section IV goes into details on the control scheme. Section V illustrates the experimental results from the real-world flights. Section VI provides the exploratory discussions of this study. Finally, Section VII concludes this article.

II. Related Work

Despite various approaches in the existing studies to enhance the operation accuracy of the aerial manipulator including structure design, precise UAV control, and precise manipulator control, there has yet to emerge a scheme to achieve millimeter-level operation task. In this section, we briefly elaborate on some of the related works regarding improving the control performance of aerial manipulator.

A. Related Work for Structure Design

A general avenue to address this problem is to design a new mechanism for improving the control accuracy of the end-effector. Delta manipulators, driven by planar linkages, have been explored due to their compact design and low inertia. For example, the lightweight delta manipulator is integrated into a standard quadrotor to eliminate the fluctuation of the moving platform [4], [5], [6]. Inspired by the origami's folding mechanism, a delta articulated arm is mounted on the front of the aerial platform to actively compensate the unwanted base fluctuation [7]. Although the accuracy of the end-effector is enhanced with the parallel structure, the workspace is limited to the cramped area, which is typically much lower as compared to a serial manipulator arm. In an attempt to address the challenges of precise aerial manipulation and limited workspace, a fully actuated aerial manipulator is presented [10]. The improved aerial manipulator, composed of a parallel 3 degree-of-freedom (DOF) manipulator and an omnidirectional tilt-rotor, can achieve an end-effector tracking error of less than 2 cm. The omnidirectional aerial platform appears popular for force contact task [8], [9], [11]. Similar to parallel delta structure, the dual manipulator system is introduced in [12] and [13]. With the help of the reaction effect, the multiarm mechanism allows the partial cancellation of the coupling disturbances induced by the one arm over the aerial platform. Nevertheless, the probability of collision is greatly increased due to the complex structure. It is nontrivial to ensure safety when conducting aerial manipulation tasks.

B. Related Work for Precise UAV Platform Control

On the premise of retaining the original mechanical structure, it is a good option to develop advanced control scheme to improve the flight performance of the aerial platform. A plethora of algorithms and controllers are dedicated, while the strong coupling effects are either compensated or suppressed. On the basis of the forward dynamics, a virtual motion decomposition method is proposed to allow the 2-DOF manipulator to operate in the x–z plane [14]. In [15], a variable inertia model is utilized to estimate the dynamic coupling effects between the hexarotor and 2-DOF manipulator. To overcome the dynamic model coupling effects, a robust controller is developed to enhance the flight performance of the UAV platform in the presence of the manipulator movement. With respect to the dynamic uncertainties from the quadrotor, robotic arm, and payload, the adaptive control scheme is presented to enable aerial manipulator to pick objects successfully [16], [17]. It is interesting that a reinforcement learning approach is employed to ensure minimal coupling effects on the quadrotor dynamics [16]. The impressive tracking performance can be achieved using the incremental nonlinear dynamic inversion (INDI) method [31], which directly compensates external disturbances, whereas, the INDI method highly relies on direct motor speed feedback using additional sensors like optical encoders [31] and radar systems [32] to rapidly estimate external disturbances, which is difficult to apply to other aerial manipulators.Another basic idea is to estimate the uncertainty by way of the induced influence on the system performance. In [18] and [19], the standard singular perturbation method is presented to ensure the stability of the aerial manipulator while a disturbance observer (DO) is employed to estimate the coupling effects. A novel control approach that consists of extended state observers (ESOs) and cascade controllers is reported to ensure the control performance of the UAV platform [20]. Some works in precise control of aerial manipulators adopt coupled control schemes [30], [33], where the aerial manipulator is considered as a unique entity. Furthermore, the implementation of coupled controller depends on the real-time computation of the dynamic model. Due to the "dimensional explosion" problem of inertia matrix, the method may not be feasible for complex aerial manipulators.

In our control scheme, the fluctuation of the aerial platform is directly negated by transforming the reference trajectory of the manipulator, so as to achieve precise end-effector control. Therefore, the classical proportion-integration-differentiation (PID) control scheme is employed to ensure the stability of the the UAV platform, reducing the complexity of controller.

C. Related Work for Precise Manipulator Control

Different from improving the flight accuracy of the UAV platform, the concept of precise manipulator control focuses on exploiting the control ability of the manipulator to cope with the floating-base disturbance. In [14], [20], [23], a classical error feedback-based method is employed to enhance the control performance of the end-effector. However, the conventional method may be insufficient for the accuracy requirement subject to the floating-base disturbance. As an extension of feedback control, a potential field-based control scheme is able to improve the control accuracy [24]. The floating-base disturbance is directly suppressed using additional sat function term, at the cost of chattering of the manipulator. Another possible solution to address the fluctuation of the aerial platform is to directly plan the manipulator joint position. With the recomputed input joint positions, the end-effector of the delta manipulator can compensate for the UAV offsets [5]. Moreover, a joint position reference generation method is developed in [25], where a correct term is added to adjust the joint position. By this means, it can alleviate the effect of the floating-base disturbance on the position error of the end-effector. However, the calculation of the replanned signals relies on the accurate inverse kinematic algorithm. The motion tracking problem of the manipulator placed on a massive base such as a ship is discussed in [26], [27], and [28], which plan the manipulator states to compensate for the undesired base motion. Nevertheless, the strict assumption that the inertia of the base must be larger than that of the manipulator is not valid for aerial manipulator. Moreover, the discontinuous velocity signal may cause the protective stop of the manipulator, which impedes the control accuracy of the end-effector. Our control scheme exploits the further motion information of the UAV platform to replan the reference trajectory of the manipulator. Subsequently, an optimization controller is developed to track the reference trajectory by incorporating practical constraints of aerial manipulator.

III. Problem Formulation

In this section, we introduce a control scheme and a detailed analysis of the mechanical layout and the kinematic relationship to achieve millimeter-level pick and peg-in-hole tasks.

As illustrated in Fig. 1, four coordinate frames are defined to describe the kinematics of aerial manipulator: the inertial reference frame $\mathcal{F}_I$, the UAV body-fixed frame $\mathcal{F}_B$, the manipulator base-fixed frame $\mathcal{F}_\Delta$, and the pose frame attached to the manipulator end-effector $\mathcal{F}_E$. There is only one constant position deviation P_Δ between $\mathcal{F}_\Delta$ and $\mathcal{F}_B$. The symbols are listed in Table I for the convenience of the following discussion.

A. Kinematic Model of the Manipulator

As shown in Fig. 1, the 5-DOF manipulator consists of four joint links and a grasping gripper. In robot analysis, kinematics is a fundamental and critical concept, which describes the relationship between the end-effector motion and the joint displacements. Both the Denavit–Hartenberg (D–H) convention [34] and the screw-based method [23] are widely adopted in the community. However, the D–H model may be discontinuous when the consecutive joint axes are nearly parallel [35]. Rather than treating the motion of the manipulator as a set of frame transformations, the screw-based method regards the motion as a kinematic chain of joint twists with respect to the initial state of the manipulator. By virtue of the product of exponentials (POE) formula, the geometric nature of the manipulator can be explicitly expressed. Fig. 2 shows the screw convention of the manipulator kinematic geometry. Let $\omega_i \in \mathbb{R}^3$ and $v_i \in \mathbb{R}^3$ represent the unit angular velocity and linear velocity of the ith joint, respectively. $r_i \in \mathbb{R}^3$ denotes the position of any point attached on the ith joint axis. According to the screw theory [23], the body twist can be expressed in the $Pl\ddot{u}cker$ coordinate as

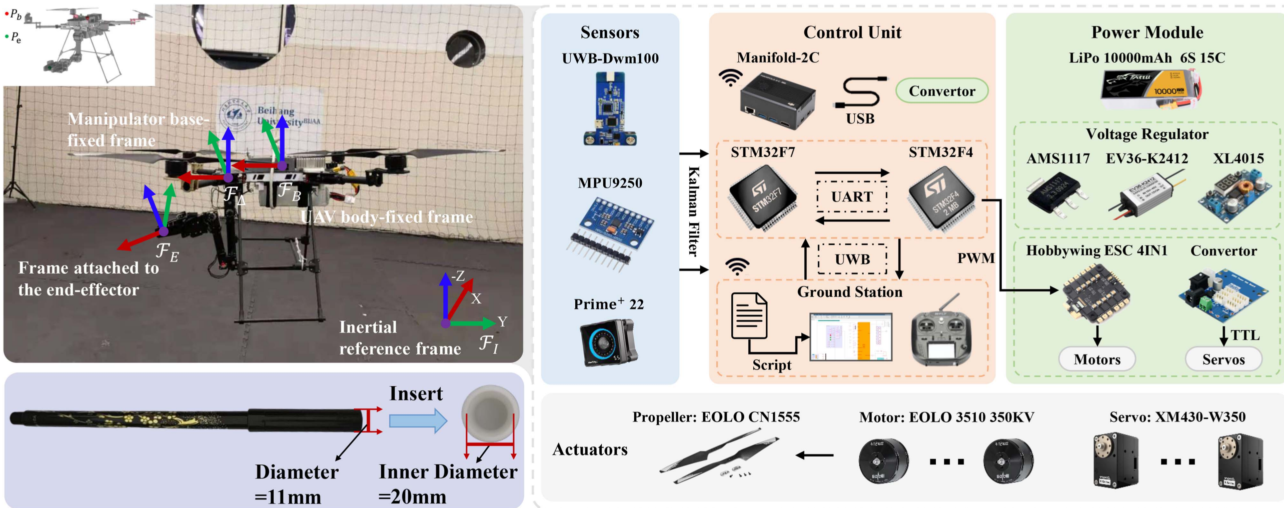

Fig. 1. Left: Schematic of aerial manipulator and millimeter-level pick and peg-in-hole task. Right: aerial manipulator hardware structure.

TABLE I
NOMENCLATURE

Symbols	Physical Intepretations
$P_e \in \mathbb{R}^3$	the position of the end-effector, expressed in $\mathcal{F}_I$
$P_b \in \mathbb{R}^3$	the center of gravity position of the UAV platform, expressed in $\mathcal{F}_I$
$P_\Delta \in \mathbb{R}^3$	the position of the manipulator base with respect to P_b, expressed in $\mathcal{F}_B$ (Fixed Value $[0.11, 0, 0.03]^\top$)
$\eta = [\eta_\phi \quad \eta_\theta \quad \eta_\psi]^\top$	the attitude Euler angles of the UAV platform (roll pitch yaw)
$\omega_b = [\omega_p \quad \omega_q \quad \omega_r]^\top$	the angular velocities of the UAV platform in $\mathcal{F}_B$
$P_{e\iota}^\Delta \in \mathbb{R}^3$	the position of the end-effector with respect to its base, expressed in $\mathcal{F}_\Delta$
$V_{e\iota}^\Delta \in \mathbb{R}^3$	the velocity of the end-effector with respect to its base, expressed in $\mathcal{F}_\Delta$
$\boldsymbol{R}_B^I \in \mathbb{R}^{3\times3}$	the attitude rotation matrix from $\mathcal{F}_B$ to $\mathcal{F}_I$
$\boldsymbol{R}_E^I \in \mathbb{R}^{3\times3}$	the attitude rotation matrix from $\mathcal{F}_E$ to $\mathcal{F}_I$
$\boldsymbol{R}_E^\Delta \in \mathbb{R}^{3\times3}$	the attitude rotation matrix from $\mathcal{F}_E$ to $\mathcal{F}_\Delta$
$\boldsymbol{R}_\Delta^B \in \mathbb{R}^{3\times3}$	the attitude rotation matrix from $\mathcal{F}_\Delta$ to $\mathcal{F}_B$ (identity matrix)
$\boldsymbol{I}_{n\times m}/\boldsymbol{0}_{n\times m} \in \mathbb{R}^{n\times m}$	the matched identity matrix/the zero matrix
$\boldsymbol{J}(q) \in \mathbb{R}^{m\times5}$	the Jacobian matrix from the end-effector to its base frame (m $\leq$ 5)
$q \in \mathbb{R}^5$	the joint position of the manipulator
$e_3 = [0 \quad 0 \quad 1]^\top$	the unit vector
$g = 9.81$	the acceleration of gravity

$\xi_i \in \mathbb{R}^6$ and it can be calculated as

$$\xi_i = \begin{bmatrix} \omega_i \\ v_i \end{bmatrix} = \begin{bmatrix} \omega_i \\ r_i \times \omega_i \end{bmatrix}. \tag{1}$$

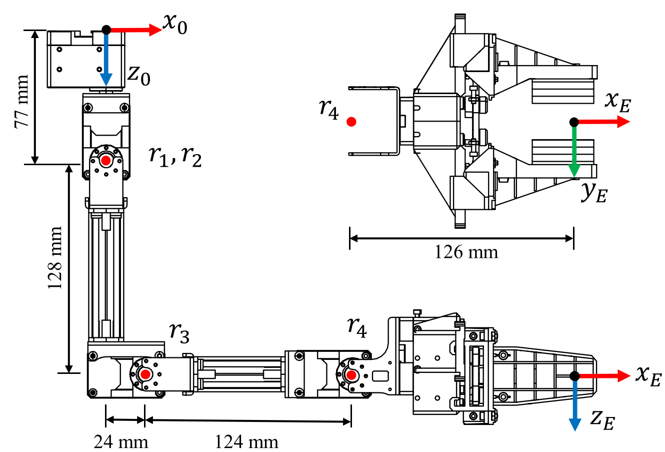

Fig. 2. Modeling of the manipulator using the screw-based method.

$\check{\boldsymbol{\xi}}_{\boldsymbol{i}} \in se(3)$ is the Lie algebraic form of ξ_i, which can be expressed as

$$\check{\boldsymbol{\xi}}_{\boldsymbol{i}} = \begin{bmatrix} \boldsymbol{\omega}_{\boldsymbol{i}}^\times & v_i \\ 0_{3\times1} & 1 \end{bmatrix}. \tag{2}$$

As a convention, $(\cdot)^\times$ denotes the skew-symmetric operator of a vector. By incorporating the matrix form of twist $\check{\xi}_i$, the exponential mapping $\boldsymbol{\Theta}_{\boldsymbol{i}} = e^{q_i \check{\boldsymbol{\xi}}_{\boldsymbol{i}}} \in \mathbb{R}^{4\times4}$ can be obtained via Rodriguez formula

$$\boldsymbol{\Theta}_{\boldsymbol{i}} = \begin{bmatrix} e^{q_i \boldsymbol{\omega}_i^\times} & (\boldsymbol{I}_{\boldsymbol{3\times3}} - \boldsymbol{e}^{\boldsymbol{q_i \omega_i^\times}})(\omega_i \times v_i) + q_i \omega_i \omega_i^\top v_i \\ 0_{3\times1} & 1 \end{bmatrix} \tag{3}$$

where q_i represents the ith joint position of the manipulator. Therefore, the forward kinematics of the manipulator can be represented by the product of a cluster of exponential mappings of the joint twists and the initial homogenous transformation

TABLE II
POE Parameters and Inertia Parameters of the Manipulator

Joint	ω_i	r_i (m)	mass (kg)
1	$\begin{bmatrix}0 & 0 & 1\end{bmatrix}^\top$	$\begin{bmatrix}0 & 0 & 0.077\end{bmatrix}^\top$	0.210
2	$\begin{bmatrix}0 & 1 & 0\end{bmatrix}^\top$	$\begin{bmatrix}0 & 0 & 0.077\end{bmatrix}^\top$	0.146
3	$\begin{bmatrix}0 & 1 & 0\end{bmatrix}^\top$	$\begin{bmatrix}0.024 & 0 & 0.205\end{bmatrix}^\top$	0.138
4	$\begin{bmatrix}0 & 1 & 0\end{bmatrix}^\top$	$\begin{bmatrix}0.148 & 0 & 0.205\end{bmatrix}^\top$	0.236

matrix

$$\boldsymbol{T}_{\boldsymbol{E}}^{\boldsymbol{\Delta}} = \boldsymbol{\Theta_1} \cdots \boldsymbol{\Theta_4} \boldsymbol{T_0} \tag{4}$$

where $\boldsymbol{T_0} \in \mathbb{R}^{4\times 4}$ is a known transformation matrix from the end-effector to its base frame when the manipulator is in the initial configuration. Moreover, Jacobian matrix $\boldsymbol{J}(q)$ can be calculated by the joint twists and the exponential mappings of the joint twists as

$$\boldsymbol{J}(q) = \left[\xi_1^*, \ldots, \xi_4^*\right] \tag{5}$$

where ξ_i^* denotes the unit screw of the ith joint in current manipulator configuration. It can be obtained as

$$\xi_i^* = Ad(\boldsymbol{\Theta_1} \cdots \boldsymbol{\Theta_{i-1}})\xi_i \tag{6}$$

where $Ad(\cdot)$ denotes the adjoint transformation of a matrix. The main advantages of the POE formula are the geometric nature and the general modeling framework. Only the initial transformation matrix $\boldsymbol{T}_0$ and the joint twists $\boldsymbol{\Theta_i}$ evaluated with respect to the base frame $\mathcal{F}_\Delta$ are required to derive the forward kinematics. The screw parameters and inertia parameters of the manipulator are listed in Table II.

B. Design Consideration

The layout of aerial manipulator should be reasonable to expand current capability and accomplish millimeter-level operation tasks. In an attempt to improve the accuracy of the end-effector, the delta-type manipulators are exploited to compensate the fluctuation of the aerial platform [4], [5], [6]. In contrast to parallel manipulators with limited workspace, serial manipulators in general have the advantages of dexterity and large operation range. Given most small-scale UAVs with limited payloads, low-complexity and lightweight grippers may be suitable [1], [36], [37]. Due to the low-complexity, these grippers are usually attached directly to the aerial platform. The relatively simple structure implies that the grippers can hardly compensate the undesired fluctuation of the aerial platform.

In this article, the designed aerial manipulator mainly consists of a quadrotor UAV with an X-shaped rotor arm configuration and a 5-DOF manipulator with a gripper, as illustrated in Fig. 1. With respect to traditional layout of aerial manipulator [15], [19], [25], the battery and the manipulator are integrated at the center of the UAV platform to alleviate the shift of the center-of-mass (CoM) of overall system. However, the airflow generated by the propeller has an adverse impact on operating missions. In addition, the workspace of the manipulator is restricted below the UAV platform, limiting its applications in a wide range.

The study of workspace is essential for the optimal placement of work piece and the realization of high dexterity of manipulator [38]. A novel layout is designed to attenuate the airflow effect, as shown in Fig. 3. The manipulator is placed at the front part of the UAV platform. The battery is located at the back part of the UAV platform to partially compensate the shift of CoM. By resorting to this layout, the task space of aerial manipulator can be expanded and the effect of the airflow can be attenuated. In fact, the manipulator is subject to multiple constraints such as propeller protection, joint limitation, and collision avoidance with the UAV frame. To model the reachable space, the manipulator motions are analyzed by testing systematically displacements of its joints. A total of 20 000 joint positions are randomly sampled within their respective joint limits. This yields a total of about 12 000 feasible positions of the end-effector. The resulting reachable-space samples for the manipulator are illustrated in Fig. 3(e). Meanwhile, Fig. 3(b)–(d) demonstrates the generated feasible sample points in three planes. Fig. 3(f)–(h) depicts the probability distribution of these positions that is modeled by using kernel density estimation method along three different planes.

C. Analysis of the Kinematic Error Amplification Effect

In real-world scenarios, a flying UAV must be considered as a floating platform with both translational and orientational offsets. In order to fully excavate the influence of the floating-base disturbance, the kinematic transfer effect is quantified. First, the kinematics of the aerial manipulator is given as

$$\begin{aligned} P_e &= P_b + \boldsymbol{R}_B^I P_\Delta + \boldsymbol{R}_B^I \boldsymbol{R}_\Delta^B P_{e\iota}^\Delta \\ \boldsymbol{R}_e &= \boldsymbol{R}_B^I \boldsymbol{R}_\Delta^B \boldsymbol{R}_E^\Delta. \end{aligned} \tag{7}$$

Equation (7) illustrates that the position of the end-effector is composed of two portions: the controllable part of the UAV platform (P_b and $\boldsymbol{R}_B^I$), and the controllable part of the manipulator $P_{e\iota}^\Delta$. The rotation matrix $\boldsymbol{R}_B^I$ can be formulated as

$$\boldsymbol{R}_B^I = \begin{bmatrix} C_\psi C_\theta & C_\psi C_\theta S_\theta - S_\psi C_\phi & C_\psi S_\theta C_\phi + S_\psi S_\phi \\ S_\psi C_\theta & S_\psi S_\theta S_\theta + C_\psi C_\phi & S_\psi S_\theta C_\phi - C_\psi S_\phi \\ -S_\theta & C_\theta S_\phi & C_\theta C_\phi \end{bmatrix} \tag{8}$$

where S_x and C_x denote sin$x$ and cos$x$, respectively. Equations (7) and (8) imply that there exists a strong nonlinear coupling in the kinematic level on account of the trigonometric function. In addition, due to the multilink structure of the manipulator, the pose deflection of the UAV platform would dramatically affect the end-effector position. Suppose that the maximum tracking errors of the aerial platform are 3 cm in position and 5° in attitude. According to (7), even if the UAV platform shakes slightly, the position deviation of the end-effector is amplified considerably. To be more specific, the error ranges of the end-effector are amplified to -5.5–5.0 cm, -8.0–8.1 cm, and -6.1–6.2 cm along x, y, and z axis, respectively. The amplification effect is visualized in Fig. 4. Notice that the pose deviation of the end-effector is not completely symmetrical due

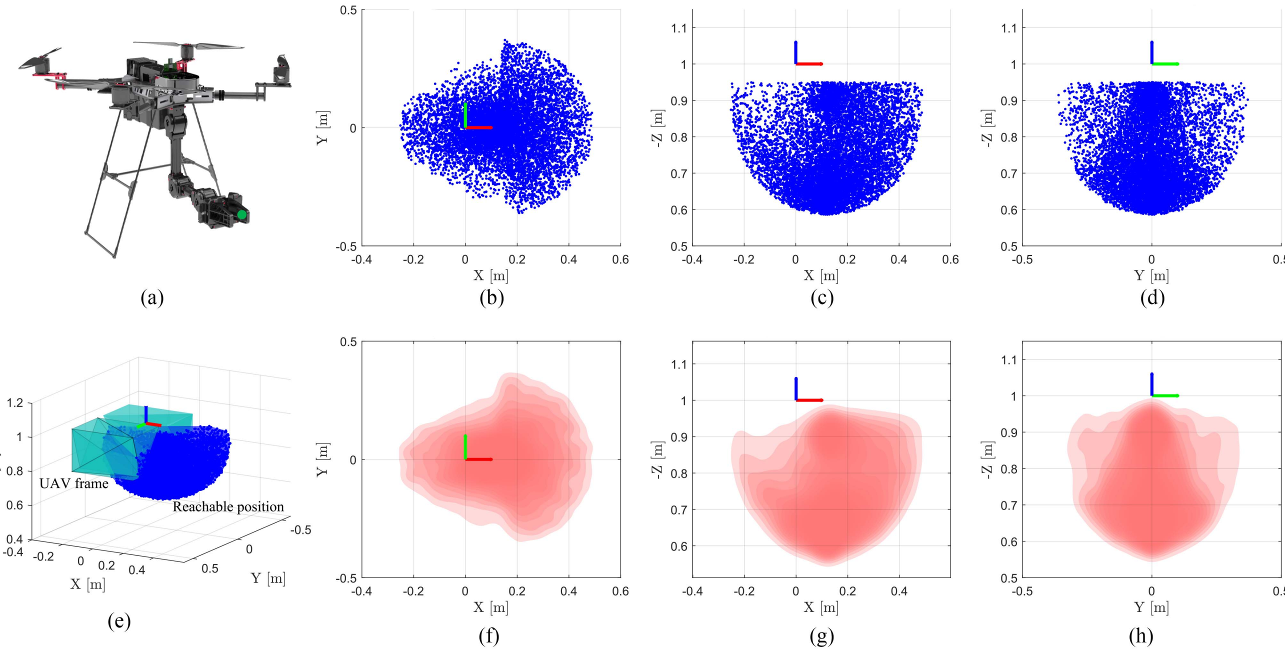

Fig. 3. Modeling of the reachable space for the end-effector. (a) Schematic diagram of the aerial manipulator. (b) Samples x–y plane. (c) Samples x–z plane. (d) Samples y–z plane. (e) Workspace visualization of the end-effector in $\mathcal{F}_I$ (The light green shades represent the side border). (f) Model x–y plane. (g) Model x–z plane. (h) Model y–z plane.

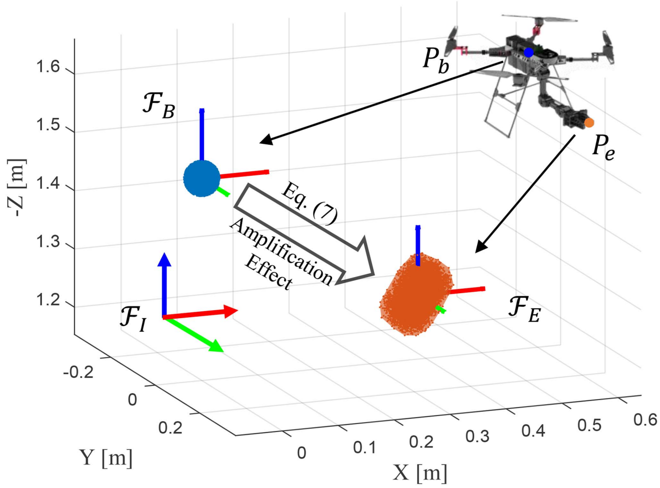

Fig. 4. Schematic representation of the kinematic error amplification effect while the manipulator is in initial state ("L" configure).

to the nonlinearity of the rotation matrix and the limit of the reachable space.

D. Analysis of the Floating-Base Disturbance

It is of utmost importance and a significant challenge to develop high-performance and reliable control strategies. The high flexibility of the serial manipulator should be fully utilized to tackle the floating-base disturbance. For the sake of understanding, (7) is rewritten as a homogeneous transformation formula

$$\boldsymbol{T}_E^I=\boldsymbol{T}_B^I\boldsymbol{T}_\Delta^B\boldsymbol{T}_E^\Delta=\begin{bmatrix}\boldsymbol{R}_B^I\boldsymbol{R}_\Delta^B\boldsymbol{R}_E^\Delta & P_b+\boldsymbol{R}_B^I(P_\Delta+\boldsymbol{R}_\Delta^B P_{e\iota}^\Delta)\\ \boldsymbol{0}_{1\times 3} & 1\end{bmatrix}. \tag{9}$$

As shown in (9), the position and attitude of the end-effector in $\mathcal{F}_I$ are represented by three elements: the fluctuation portion of the UAV $\boldsymbol{T}_B^I$, the constant deviation portion $\boldsymbol{T}_\Delta^B$, and the adjustment portion of the manipulator $\boldsymbol{T}_E^\Delta$. By this means, it is potential to maneuver the manipulator to counteract the UAV fluctuation. It is intuitive that if the motion of the UAV platform $\boldsymbol{T}_B^I$ can be predicted, a modified trajectory $\hat{\boldsymbol{T}}_\Delta^E$ with respect to $\mathcal{F}_\Delta$ can be generated for the manipulator. By tracking the improved trajectory, the floating-base disturbance can be addressed.

Given the prediction of the UAV platform at the ith step ahead, $\hat{\boldsymbol{T}}_B^I(t+i)$, the desired end-effector trajectory defined in $\mathcal{F}_I$ can be modified to the manipulator base frame $\mathcal{F}_\Delta$.

$$\hat{\boldsymbol{T}}_E^\Delta(t+i)=\boldsymbol{T}_B^\Delta\hat{\boldsymbol{T}}_I^B(t+i)\boldsymbol{T}_E^I(t+i), i=1,\ldots,N. \tag{10}$$

Consequently, the trajectory tracking problem in $\mathcal{F}_I$ can be regarded as holding the transformed trajectory with respect to the frame $\mathcal{F}_\Delta$. By this means, as long as the future state of the UAV platform is available, the floating-base disturbance can be thoroughly dealt with. However, it is difficult to accurately model the UAV motion due to the presence of multiple disturbances. Therefore, obtaining accurate future motion state of the UAV platform is crucial, which will be discussed in Section IV-A.

E. Analysis of the Manipulator Control

In this article, the manipulator is a 5-DOF complex multijoint mechanical system. Let $\epsilon \in \mathbb{R}^m$ be the pose of the end-effector in the base frame $\mathcal{F}_\Delta$, which is related to joint position q

$$\epsilon = h(q) \tag{11}$$

where $h : \mathbb{R}^5 \to \mathbb{R}^m$ is the mapping from joint space to task space. Differentiating (11) yields the mapping relationship between the end-effector velocity and joint velocity

$$\dot{\epsilon} = \boldsymbol{J}(q)\dot{q} \tag{12}$$

where $\boldsymbol{J}(q) \in \mathbb{R}^{m\times 5}$ is the Jacobian matrix for the manipulator at current configuration. The most common approach is to use the inverse of $\boldsymbol{J}(q)$ to calculate the required joint velocity [25], [39]

$$\dot{q} = \boldsymbol{J}(q)^{-1}\dot{\epsilon}. \tag{13}$$

However, the inverse matrix $\boldsymbol{J}(q)^{-1}$ only exists when $\boldsymbol{J}(q)$ is square and nonsingular. For redundancy control ($m \leq 5$), $\boldsymbol{J}(q)$ is not square and no unique solution exists for (13). Hence, given the desired end-effector trajectory ϵ in the task space, the Moore–Penrose pseudoinverse of $\boldsymbol{J}(q)$ is utilized to obtain the desired joint velocity in practice [26], [40]

$$\dot{q} = \boldsymbol{J}(q)^{\dagger}\dot{\epsilon} \tag{14}$$

where $(\cdot)^\dagger$ denotes the Moore–Penrose pseudoinverse operator of a matrix. The Moore–Penrose pseudoinverse can find $\dot{q}$ with the minimum Euclidean norm. In particular, when $\boldsymbol{J}(q)$ has linearly independent rows ($\boldsymbol{J}(q)\boldsymbol{J}(q)^\top$ is square and invertible), the Moore–Penrose pseudoinverse of $\boldsymbol{J}(q)$ can be formulated as

$$\boldsymbol{J}(q)^\dagger = \boldsymbol{J}(q)^\top(\boldsymbol{J}(q)\boldsymbol{J}(q)^\top)^{-1}. \tag{15}$$

Therefore, the pseudoinverse of $\boldsymbol{J}(q)$ always exists and can yield an accurate solution for (14). Nonetheless, if the desired signal $\dot{\epsilon}$ is discontinuous and abrupt, the excessive signal $\dot{q}$ cannot be used as an input to the manipulator dynamic controller. The reason lies in that the protective stop of the low-level manipulator dynamic controller would be triggered. To circumvent this problem, commands sent to the controller have to be reduced [26], degrading the tracking performance. Furthermore, safety issues should be considered when aerial manipulator is operating. The manipulator must be operated within a safe range, underside of the propellers and inner side of the UAV's outer frame. Therefore, this study focuses on optimizing the acceleration signal of the end-effector $\ddot{\epsilon}$ in the task space, by taking into account multiple practical constraints, including control action smoothness, kinematic feasibility, actuators limitation, and dynamical constraint.

Driven by above analysis, in order to achieve high-precision operation tasks under floating-base disturbance, in summary, two technical aspects are of concern.

1) Efficiently and accurately forward forecast the UAV platform motion $\hat{\boldsymbol{T}}_B^I(t+i)$ for given prediction horizon $i = 1, \ldots, N$. Therefore, the desired trajectory can be modified by (10) to dissolve the floating-base disturbance.
2) Seek the optimized control sequence of the end-effector $\ddot{\epsilon}(t), \ldots, \ddot{\epsilon}(t+N-1)$ in the task space to track the modified trajectory $\hat{\boldsymbol{T}}_E^\Delta(t+i)$ by considering multiple constraints.

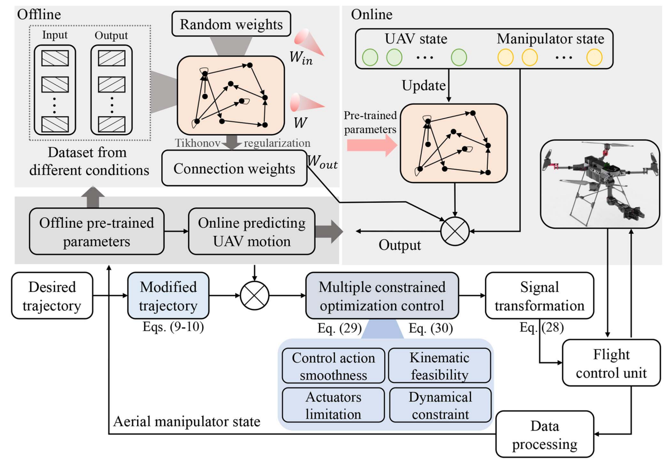

Fig. 5. System diagram.

IV. Control Architecture

The design procedure of predictive optimization scheme is presented, as illustrated in Fig. 5. First, the coupling dynamic model of the aerial manipulator is established. Second, a learning-based prediction method is exploited to rapidly forecast the UAV platform motion by incorporating pretrained parameters. Based on the UAV motion prediction information, a multiple constrained optimization control strategy is developed to achieve millimeter-level control accuracy of the end-effector.

A. Motion Prediction of the UAV Platform

The first key problem is to accurately and efficiently predict the motion of the UAV platform. As shown in (7), in order to ensure the manipulator can accurately achieve millimeter-level operations, the UAV platform in general is requested in a quasi-static manner, that is, the velocity vector $\dot{P}_b$ should be equal to 0 [3], [13], [41]. However, due to the presence of unavoidable perturbations, both translational and orientational offsets of the aerial platform are present in practice.

As seen in Fig. 1, the CoM of the aerial manipulator can only be partially compensated by the battery located at the rear of the UAV platform. The CoM is constantly changing with the manipulator motion. The model uncertainties have a significant impact on the control accuracy of the UAV platform. Moreover, the strong dynamic coupling effects caused by the manipulator movement, further exacerbate the fluctuation of the UAV platform. According to [42], the strong dynamic coupling disturbances are highly dependent on the relative motion of the manipulator with respect to the aerial platform. As compared to a bare aerial platform, the dynamic coupling disturbances caused by the manipulation motion can be modeled as

$$F_m = -m_m\ddot{P}_b + m_m g e_3 - m_m R_B^I(\boldsymbol{\omega}_b^\times\left(\boldsymbol{\omega}_b^\times P_{bm}^B\right)$$

$$+ \dot{\boldsymbol{\omega}}_b^{\times} P_{bm}^B + 2\boldsymbol{\omega}_b^{\times} \dot{P}_{bm}^B + \ddot{P}_{bm}^B) \tag{16a}$$

$$\tau_m = -J_{mb}^B \dot{\omega}_b - \boldsymbol{\omega}_b^{\times} J_{mb}^B \dot{\omega}_b + m_m P_{mb}^B \boldsymbol{R}_I^B (g e_3 - \ddot{P}_b)$$
$$- \dot{J}_{mb}^B \dot{\omega}_b - \boldsymbol{\omega}_b^{\times} L_m^B - \dot{L}_m^B \tag{16b}$$

where m_m is the mass of the manipulator. P_{bm}^B denotes the CoM of the manipulator with respect to $\mathcal{F}_B$. F_m and τ_m represent the disturbance force and disturbance torque, respectively. J_{mb}^B is the inertia tensor of the manipulator along the body-fixed frame. L_m^B describes the angular momentum of the manipulator with respect to $\mathcal{F}_B$. The detailed analysis of the coupling disturbances can be found in https://drive.google.com/file/d/1zsbLYpyewxi7FakGNQsya3btc9Ovkqwo/view?usp=drive_link Supplementary material.

In addition to the strong coupling effects caused by the manipulator, the UAV platform suffers from other uncertainties that induce the fluctuation as mentioned in [20]. The motion of the aerial platform equipped with the manipulator can be established as

$$\begin{cases} \ddot{P}_b = \frac{1}{m_s}(-f \boldsymbol{R}_B^I e_3 + F_b + F_m) + g e_3 \\ \boldsymbol{M}(\eta)\ddot{\eta} + \boldsymbol{C}(\eta, \dot{\eta})\dot{\eta} = \tau + \tau_b + \tau_m \end{cases} \tag{17}$$

where m_s is the mass of the UAV. f and τ are the outputs of the cascaded PID controller of the UAV platform, relying on the system state. $\boldsymbol{M}(\eta)$ and $\boldsymbol{C}(\eta, \dot{\eta})$ are the positive definite inertia matrix and Coriolis matrix [43], respectively. F_b and τ_b are unmodeled disturbance force and torque exerted on the UAV platform. For convenience, let $x = [P_b, \dot{P}_b, \eta, \dot{\eta}]^{\top}$, and (17) can be rearranged as

$$\dot{x} = \varrho(x, \tau, f, d(q, \dot{q}, \ddot{q}, x)) \tag{18}$$

where $d(q, \dot{q}, \ddot{q}, x)$ represents nonlinear lump disturbance including uncertainties and the strong dynamic coupling effects. Therefore, the further motion of the UAV platform is determined by the current states of the UAV and the manipulator.

As illustrated in Section III-D, one of critical aspects is to efficiently and accurately forward forecast the UAV platform motion. However, it is nontrivial to predict the future state of the UAV motion. Two key matters are presented in (18). First, it is difficult to precisely estimate $d(q, \dot{q}, \ddot{q}, x)$. Although (16a)–(16b) describe the coupling disturbances, the accurate acquisition of variable parameters is intractable. There is no guarantee that the estimated variable parameters can match sufficiently the real one using dynamic parameter identification methods [44], [45]. Moreover, it is intractable to model the uncertainties dependent on the UAV state. In contrast to establish precise disturbance model, an alternative is the use of DO [20], [46]. Nevertheless, the DO must be constructed through dynamic model of aerial manipulator. Hence, both the disturbance estimation and state prediction may be obfuscated by uncertainties. More importantly, the estimation error would further propagate through (18), leading to the state prediction deviation. The proposed model-based methods may be infeasible to accurately forward forecast the UAV platform motion.

Apart from model-based methods, data-based approaches can be exploited to forecast the UAV platform motion. Time series approach becomes popular to directly forecast motion in the

Algorithm 1: Offline Pre-training Framework.

Initialize: Randomly generated parameters: the input connection matrix $\boldsymbol{W}_{in}$ and the recurrent connection matrix $\boldsymbol{W}$. Manually selected parameters: Size of the reservoir n, desired spectral radius ρ_d, regularization coefficient ϖ, and mixing coefficient γ;
Input;
• The state of aerial manipulator;
Output;
• The connection matrix $\boldsymbol{W}_{out}$;
Step 1: Scale the recurrent connection matrix $\boldsymbol{W}$ to meet the requirement of echo state $\boldsymbol{W} = \boldsymbol{W}\frac{\rho_d}{\ell(\boldsymbol{W})}$. $\ell(\boldsymbol{W})$ is the spectral radius of matrix $\boldsymbol{W}$;
Step 2:;
while *not at end of sampling data* **do**
  Run the ESN using the training input $\vartheta(t)$;
  $h(t) = tanh(\boldsymbol{W}_{in}\begin{bmatrix}1\\ \vartheta(t)\end{bmatrix} + \boldsymbol{W}g(t-1))$;
  Collect the corresponding activation state $g(t)$;
  $g(t) = (1-\gamma)g(t-1) + \gamma h(t)$;
  Collect the reservoir state $\Xi(t)$;
  $\Xi(t) = \begin{bmatrix}1 & \vartheta(t) & g(t)\end{bmatrix}^{\top}$;
end
c **Step 3**: Collect the training output $\boldsymbol{Y}$ and compute the connection matrix $\boldsymbol{W}_{out}$;
$\boldsymbol{W}_{out} = \boldsymbol{Y}\Xi^{\top}(\Xi\Xi^{\top} + \varpi\boldsymbol{I})^{-1} \leftarrow min||\boldsymbol{W}_{out}\Xi - \boldsymbol{Y}||_2^2$

existing studies, such as AR model [26] and fourier series [47], [48]. However, a strict premise of these methods is that the manipulator motion will not affect the base platform. The rigorous assumption no longer holds for aerial manipulator with strong coupling effects.

An alternative, and increasingly popular, approach is the use of the learning-based prediction methods. Instead of exploiting the historical state of the UAV, echo state network (ESN) is expected to estimate the nonlinear model by learning the causality between state and motion [49], [50]. In comparison to the traditional neural network, ESN is widely used due to the simple training process and efficient learning algorithm. Specifically, the input signals from a low-dimensional space are mapped to a high-dimensional state space. In the high dimensional state space, linear regression method can be exploited to train the network of the connection weight. Meanwhile, other connection weights are randomly generated and remain unchanged during network training stage [49]. Moreover, ESN can hold an ongoing activation and thus exhibit dynamic memory. Focusing on the aerial manipulator with highly complex nonlinear dynamics, the efficient and simple learning algorithm is appropriate to perform real-time prediction. Algorithm 1 shows the offline pretraining process.

1) Challenges Caused by Unknown External Disturbances: In the real-world, there exist some unknown factors (e.g., wind disturbance and sensor noise) that affect the motion of the UAV platform. Hence, in the process of deploying ESN model, the influence of unknown disturbances must be considered. In this work, a mixing coefficient γ is involved. The mixing coefficient γ can adjust the percentage between the output of the input pool $h(t)$ at time t and the output of the reserve pool $g(t-1)$ at time $t-1$, which is regarded as the update speed of the reservoir dynamics. The strategy can be described as

$$g(t) = (1-\gamma)g(t-1) + \gamma h(t). \tag{19}$$

This process significantly improves the ability of rejecting unknown disturbances and produces stable motion. Notice that the mixing coefficient γ should be a value between 0 and 1. Generally, a smaller value of γ emphasizes the effect of long-term memory on future motion. Therefore, even if the feedback signals are noisy, the further motion can be well predicted on the basis of the reserve pool. Nonetheless, if γ is too small, it is difficult to fine-tune the motion, reducing the robustness to abrupt changes of position. In our work, the manipulator signals q and $\dot{q}$ can be measured directly by encoders with the resolution of 0.088° and 0.229 r/min, respectively. Moreover, the signal $\ddot{q}$ can be obtained by filtering. Hence, due to the high-quality sensor data, γ is set as 0.7.

2) Online Learning for Varying Nonlinear Dynamic Process: The mixing coefficient γ improves the robustness to unknown disturbances. However, it is powerless in the case of varying nonlinear dynamics. For example, the cascaded PID controller gains are tuned from the ground station when the UAV platform is in flight (this is common in real scenarios). With respect to the varying nonlinear dynamic process, the connection weight $\boldsymbol{W}_{\text{out}}$ is desperately required to online adapt in the presence of feedbacks. Modifying $\boldsymbol{W}_{\text{out}}$ has a direct effect on the learning process. One of the popular methods is the least mean squares (LMS) algorithm [49]. LMS is a first-order stochastic gradient descent method, which can locally approximate the error surface with a hyperplane. However, the convergence performance of LMS cannot be guaranteed when the curvature of error surface varies greatly along different directions. Note that the curvature of error surface is determined by the eigenvalues of $\Xi\Xi^{\top}$.

In this work, recursive least squares (RLS) algorithm is utilized to adapt the connection weight $\boldsymbol{W}_{\text{out}}$ in real time. In contrast to the LMS, RLS has the advantages of eigenvalue insensitivity and faster convergence, which explicitly minimizes a square error at each time step. The connection weight $\boldsymbol{W}_{\text{out}}$ can be quickly adjusted by the RLS algorithm, which shows the capacity of learning varying nonlinear dynamic process [51].

With the aid of the online updating algorithm, $\boldsymbol{W}_{\text{out}}$ can be vigorously adaptive to learn the relationship between state and motion. Therefore, the ESN-RLS scheme can be suitable for varying dynamics, avoiding the retraining process offline. The brief online algorithm framework is illustrated in Algorithm 2.

3) Data Collection: It is unambiguous that the dynamic behavior of a system reflects how it changes over time, in response to different inputs and conditions. With respect to the learning-based method, the training dataset should fully capture the nonlinear dynamics. However, it is scarcely possible to collect all state information of the system. Therefore, as far as possible, the collected data should contain the important features of nonlinear dynamics to learn the mapping relationship.

Algorithm 2: Online Learning Framework.

Initialize: Auxiliary matrix $\boldsymbol{\Phi}$, the forgetting rate φ, offline pre-trained weight matrix $\boldsymbol{W}_{out}$;
Input;
• Connection weight $\boldsymbol{W}_{out}(t-1)$, auxiliary matrix $\boldsymbol{\Phi}(t-1)$, the collected reservoir state $\Xi(t-1)$, and the output $\boldsymbol{Y}(t)$;
Output;
• The updated connection weight $\boldsymbol{W}_{out}(t)$ and the updated auxiliary matrix $\boldsymbol{\Phi}(t)$;
if *new data arrives* **then**
  Step 1: Prior uncertainty;
  $\pi(t) = \boldsymbol{Y}(t) - \boldsymbol{W}_{out}(t-1)\Xi(t)$;
  Step 2:Adaptive gain;
  $\mathcal{L}(t) = \frac{\boldsymbol{\Phi}(t-1)\Xi(t)}{\varphi+\Xi^{\top}(t)\boldsymbol{\Phi}(t-1)\Xi(t)}$;
  Step 3:The auxiliary matrix update;
  $\boldsymbol{\Phi}(t) = \frac{1}{\varphi}(\boldsymbol{\Phi}(t-1) - \mathcal{L}(t)\Xi(t)^{\top}\boldsymbol{\Phi}(t-1))$;
  Step 4:The connection matrix $\boldsymbol{W}_{out}$ update;
  $\boldsymbol{W}_{out}(t) = \boldsymbol{W}_{out}(t-1) + \mathcal{L}(t)\pi(t)$
end

Focusing on the aerial manipulator, the manipulator is demanded to follow the circular trajectory to persistently excite the nonlinear dynamics for generating informative data. The reference circular trajectories are 3-D periodic that can travel in both vertical and horizontal planes. By this means, all joint dynamics of the manipulator can be excited by the 3-D reference trajectories [52]. Combined with the requirements of precision operation, the circular trajectory radius is 6 cm, basically covering the fluctuation range of the UAV platform. Meanwhile, the angular frequency of the circular trajectory increases from 0 to 1.5 rad/s. The fundamental purpose is that the important nonlinear dynamics can be fully excited. As shown in (16a)–(16b), with the increase of the angular frequency, the coupling disturbances caused by the manipulator motion become more and more severe. In an attempt to ensure that the learned model is accurate and reliable, each stage lasts 120 s to collect sufficient and informative data.

4) Evaluation Indices: Here, we set indicators to quantitatively analyze the effectiveness of different methods to predict the aerial platform motion. The prediction accuracy and the cost of computation online are mainly considered as the evaluation indices. Higher accuracy implies that the further motion state of the UAV platform can be well estimated. Meanwhile, shorter time cost indicates that higher control frequency can be achieved. In addition, to demonstrate the prediction performance of the learning-based method, some prediction methods that have been widely used are evaluated for comparison. For example, autoregression (AR) model [26], Gaussian process regression (GPR) [53], support vector regression (SVR) [54], and the linearization of the UAV dynamics [55]. The difference between SVR (Linear) and SVR (Rbf) is that the kernel function is linear function or radial basis function. ESN-RLS represents the ESN model with online RLS algorithm. All methods are compared with respect to

TABLE III
COMPARISON AMONG DIFFERENT METHODS FOR THE UAV MOTION PREDICTION AT $i = 20$ AHEAD(UNIT:MM)

Method	Testing				Training								Testing			
	0		0.2		0.45		0.7		1.0		1.2		1.3		1.5	
	MSE	STD	MSE	STD	MSE	STD	MSE	STD	MSE	STd	MSE	STD	MSE	STD	MSE	STD
AR	2.33	1.63	2.35	1.08	2.63	1.46	2.88	1.52	2.98	2.63	3.69	2.08	3.85	1.88	4.47	2.87
GPR	1.05	0.56	1.14	0.52	1.11	0.67	1.14	0.61	1.07	0.60	1.39	0.81	1.44	0.71	1.74	0.84
Model Linearization	1.42	1.07	1.66	0.79	2.13	1.02	2.36	1.31	2.45	1.82	2.82	1.49	2.97	1.01	3.13	1.67
SVR (Linear)	1.01	0.57	1.06	0.51	1.19	0.69	1.25	0.68	1.12	0.67	1.47	0.86	1.46	0.82	1.49	0.75
SVR (Rbf)	9.27	4.46	8.24	7.54	0.23	0.28	0.18	0.17	0.18	0.21	0.64	0.70	5.75	6.21	9.82	7.08
ESN	0.92	0.46	1.09	0.46	1.08	0.61	1.15	0.60	1.11	0.58	1.50	0.78	1.39	0.76	1.44	0.73
ESN-RLS	0.49	0.33	0.57	0.31	0.68	0.46	0.79	0.43	0.64	0.42	1.11	0.59	0.88	0.53	0.92	0.48

the prediction accuracy and the complexity of implementation online. With respect to the generalization ability of the compared methods, our sampling data are divided into two portions: training dataset and test dataset. The training dataset consists of four different subdatasets with different motion frequencies, which are listed in Table III. The deployment details of these methods are illustrated in https://drive.google.com/file/d/1zsbLYpyewxi7FakGNQsya3btc9Ovkqwo/view?usp=drive_link Supplementary material.

5) Evaluation Results: As shown in Table III, with the increase of the manipulator motion frequency, the prediction error of AR model races up. The reason is that as the frequency of the manipulator action increases, the coupling effects between manipulator and UAV have a more significant impact on the UAV movement. However, this method ignores the effects caused by the manipulator movement and only exploits the historical state of the UAV. Due to that the coupling effects are partially captured, the prediction performance of the model linearization method is better than linear AR approach. However, it is intractable to accurately capture uncertainties with the increase of the manipulator motion. On the one hand, it is difficult to obtain precise variable inertia parameters. More importantly, the uncertainties would further propagate through dynamic model, leading to the state prediction deviation. Owing to the overfitting phenomenon, SVR (Rbf) shows the best prediction performance on the training sub-datasets. Nevertheless, the estimation of extrapolating parts is unsatisfactory. Table III reports that the precise prediction performance can be obtained using ESN schemes. Due to the strong learning capacity for complex nonlinear dynamics, the ESN model can describe the relationship between state and motion. By incorporating the RLS algorithm, the online learning capability of ESN-RLS model for the nonlinear dynamic process is greatly enhanced. Focusing on the dynamics that is not present in training dataset, the ESN-RLS model can modify $\boldsymbol{W}_{\text{out}}$, achieving superior predictive performance.

Another important aspect is the cost of computation online. Table IV represents the time cost to forecast the UAV motion for one second duration. Since the number of support vectors is up to several thousands, the computation time of the SVR model is up to 80 ms. The RLS algorithm is mainly responsible for the resource consumption of the ESN-RLS online prediction. Since the connection weight is updated in real time, the online computation time is more than 4 ms. In contrast, since only linear calculations are involved in the ESN model, the computation time is less than 1 ms, which is much smaller than the other models. The detailed prediction performances of the ESN model and ESN-RLS model are stated in the gray areas of Tables III and IV. For a fair comparison, parameters in all methods are tuned to achieve the best performance before testing.

TABLE IV
CALCULATION TIME (IN $10^{-3}s$) TO ESTIMATE THE UAV MOTION FOR ONE SECOND DURATION

	ESN	ESN-RLS	AR	GPR	SVR (Linear)	SVR (Rbf)	Model Linearizatin
Min	0.88	4.53	8.36	28.84	80.30	86.21	6.29
Mean	0.99	4.65	8.56	29.26	83.08	86.86	6.78
Max	1.17	4.95	8.9	30.07	86.06	87.26	7.84

TABLE V
MEAN ABSOLUTE ERROR USING ESN MODEL

Forecast Horizon	X(mm)	Y(mm)	Z(mm)	Roll(deg)	Pitch(deg)	Yaw(deg)
$N = 5$	0.49	0.38	0.21	0.46	0.22	0.23
$N = 10$	0.63	0.53	0.31	0.55	0.29	0.26
$N = 15$	0.79	0.65	0.39	0.58	0.32	0.28
$N = 20$	0.99	0.78	0.47	0.59	0.33	0.30

Table V shows the mean prediction errors of different forecast horizons when the angular frequency of the circular trajectory is 1.5 rad/s. The average position errors are less than 1.3 mm in magnitude, while the maximum orientation error is less than 0.6° for all three DOFs at $N = 20$ (0.06 s ahead). As indicated in Table V, the precise prediction results can be obtained using this learning-based method, providing a solid foundation to achieve high-precision control performance of the end-effector.

Remark 1: To ensure the fairness of the comparisons, all results in above tables are obtained in the same platform with Intel i7-12700H with 16 GB RAM. The codes of all models are also edited in MATLAB. In addition, the SVR model is trained by using https://www.csie.ntu.edu.tw/\,cjlin/libsvm/ LIBSVM toolbox and https://ww2.mathworks.cn/help/stats/fitrgp.html GPML toolbox is employed to train the GPR model.

B. Optimization Control of the Manipulator

The above section provides a detailed analysis about predicting the motion of the aerial platform via the learning-based method. By incorporating the prediction information, the primary concern herein is to generate control signals that conform to requirements of dissolving the floating-base disturbance by maneuvering the manipulator. On the basis of Section III-E, a strategy is developed to directly optimize the acceleration of the end-effector. Let $h = [P_{e\iota}^{\Delta} \quad V_{e\iota}^{\Delta}]^{\top}$ be the state vector of the end-effector. The propagation of the end-effector state $h_i = [P_{e\iota}^{\Delta} \quad V_{e\iota}^{\Delta}]_i^{\top}$ in discrete time can be expressed as a second-order system

$$\begin{cases} h_{i+1} = \boldsymbol{A}h_i + \boldsymbol{B}u_i \\ y_{i+1} = \boldsymbol{C}h_{i+1} \end{cases} \tag{20}$$

where u_i represents the acceleration of the end-effector and

$$\begin{cases} \boldsymbol{A} = \begin{bmatrix} \boldsymbol{I}_3 & \delta t \boldsymbol{I}_3 \\ \boldsymbol{0}_3 & \boldsymbol{I}_3 \end{bmatrix} \quad \boldsymbol{B} = \begin{bmatrix} \frac{1}{2}\delta t^2 \boldsymbol{I}_3 \\ \delta t \boldsymbol{I}_3 \end{bmatrix} \\ \boldsymbol{C} = \begin{bmatrix} \boldsymbol{I}_3 & \boldsymbol{0}_3 \end{bmatrix} \end{cases}. \tag{21}$$

Note that δt is the control period. By combining (10) and (20), the tracking error of the manipulator for the modified future trajectory can be described as

$$\hat{e}_p(t+i) = \hat{y}_{\Delta}(t+i) - y(t+i) \tag{22}$$

where $\hat{y}_{\Delta}$ represents the modified trajectory in $\mathcal{F}_{\Delta}$, which is the position part of $\hat{\boldsymbol{T}}_E^{\Delta}(t+i)$. As a consequence, the objective is to find the optimal control sequence $u(t+j)$ for $j = 0, \ldots, N-1$ that can minimize the position error of the end-effector across the forecast horizon $i = 1, \ldots, N$. Therefore, the precise operation problem of aerial manipulator is formulated to seek an optimal control input u to minimize the following error cost function:

$$Q_1 = \|\hat{e}_p\|^2_{\boldsymbol{\Lambda}_1} = \hat{e}_p^{\top}\boldsymbol{\Lambda}_1\hat{e}_p, \quad \hat{e}_p \in \mathbb{R}^{3N\times 1} \tag{23}$$

where $\boldsymbol{\Lambda}_1 \in \mathbb{R}^{3N\times 3N}$ is a positive-definite weighting matrix. Without any constraints, (22) can be simplified to an unconstrained quadratic programming problem. The unique analytical solution can be quickly computed. However, such a purely unconstrained problem does not adequately take into account the practical safety during executing operation tasks. With respect to the aerial manipulator, specific constraints are of seminal importance that must be considered in the controller design.

Control Action Smoothness: The smoothness of control action u should be a major factor in saving energy and protecting the actuators. This can help reduce sharp acceleration maneuvers that may result from abrupt external impulse acting on aerial manipulator. For such a consideration, following cost function toward optimal control input u is considered

$$Q_2 = \|\Delta u\|^2_{\boldsymbol{\Lambda}_2} = \Delta u^{\top}\boldsymbol{\Lambda}_2\Delta u, \quad \Delta u \in \mathbb{R}^{3N\times 1} \tag{24}$$

where $\boldsymbol{\Lambda}_2 \in \mathbb{R}^{3N\times 3N}$ is a positive-definite weighting matrix and Δu represents the increment of control action at each step.

Kinematic Feasibility: In contrast to the conventional fixed-base robots, the manipulator is mounted on the undercarriage of the UAV platform. Therefore, the effective task space of the end-effector is restricted to the underside of the propellers and the inner side of the UAV outer frame, as depicted in Fig. 3. To ensure the efficacy and safety, it is, mandatory to consider the kinematic feasibility of aerial manipulator when executing operation tasks. The kinematic cost Q_3 is formulated as the accumulated L_2 distance to the safe border along the axis, which is expressed as

$$Q_3 = \lambda_3 \sum_{i=1}^{N} F(d(y(t+i))) \tag{25}$$

where λ_3 is a positive-definite weighting parameter. $d(y(t+i)$ is the closest distance between $y(t+i)$ to the border of work space. F is defined as

$$F(d(y(t+i))) = \begin{cases} (d(y(t+i) - d_0)^2, & d(y(t+i) \le d_0 \\ 0, & d(y(t+i) \ge d_0 \end{cases} \tag{26}$$

where d_0 is the safe distance. The involvement of d_0 can not only ensure the manipulator to work in an adequate space, but also guarantee the safety of operations.

Actuators Limitation: In this study, DYNAMIXEL XM-430 servo actuators are employed to drive manipulator with a stall torque of 4.1 N · m. Safety is a critical aspect of performing graceful performance. Thus, actuators should always be driven in a safe state in accordance with the capability of the manipulator. Here, an additional actuators limitation cost is designed. Specifically, the acceleration of the end-effector should be restricted as

$$u_{\min} \le u \le u_{\max} \tag{27}$$

where $u_{\min}$ and $u_{\max}$ indicate the allowable minimum and maximum accelerations of the manipulator end-effector in the task space.

Dynamical Constraint: It should be emphasized that the dynamic feasibility of the manipulator joint is of concern for real-time control. For the sake of feasibility, aerial manipulator must obey joints limitation across entire control period. Therefore, the joint position should be constrained to a feasible region as

$$\begin{gathered} q_{\min} \le q(t+i) \le q_{\max}, i = 1, \ldots, N \\ q(t+i) = q(t) + \sum_{j=0}^{i-1} \delta t(\boldsymbol{J}_v^{\dagger} v(t+j) - \varsigma\Delta q) \end{gathered} \tag{28}$$

where $q_{\min}$ and $q_{\max}$ are the lower and the upper bounds of the manipulator joint position. $\boldsymbol{J}_v(q)$ is the linear velocity part of $\boldsymbol{J}(q)$. Δq represents the joint tracking error at the current time. In comparison to (12), the tracking error of manipulator joint position caused by external disturbances like downwash is compensated by adding correction term Δq.

In summary, the optimization problem is formulated as

$$\min_u Q = \min_u (Q_1 + Q_2 + Q_3) \tag{29}$$

subject to

$$\begin{cases} h_{i+1} = \boldsymbol{A}h_i + \boldsymbol{B}u_i \\ y_{i+1} = \boldsymbol{C}h_{i+1} \\ u_{\min} \le u \le u_{\max} \\ q(t+i) = q(t) + \sum_{j=0}^{i-1} \delta t(\boldsymbol{J}_v^{\dagger} v(t+j) - \varsigma\Delta q) \\ q_{\min} \le q(t+i) \le q_{\max}, i = 1, \ldots, N. \end{cases} \tag{30}$$

Q_1, Q_2, and Q_3 are penalty terms of the end-effector tracking error, the control action smoothness, and the kinematic feasibility, respectively. Therefore, the optimization problem is redefined

Algorithm 3: Predictive Optimization Scheme.

1 **Initialize**: Offline pre-trained parameters $\boldsymbol{W}_{in}$, $\boldsymbol{W}$ and $\boldsymbol{W}_{out}$; mixing coefficient γ; step size δt; weighting matrices $\boldsymbol{\Lambda}_1$ and $\boldsymbol{\Lambda}_2$; weighting parameter λ_3; safe distance d_0; actuators limitation u_{min} and u_{max}; joints limitation q_{min} and q_{max};
2 **Input**;
3 • Desired trajectory in $\mathcal{F}_I$;
4 • The state of aerial manipulator;
5 **Output**;
6 • The optimized control sequence of the end-effector;
7 **for** $t = 0$ *to* ∞ **do**
8   **if** *ESN-RLS model is utilized* **then**
9   **if** *new data arrives* **then**
10   Execute Algothrim 2;
11   **end**
12   **end**
13   Forecast the UAV motion for given horizon ;
14   Calculate modified trajectory in $\mathcal{F}_\Delta$ by Eq. (10);
15   Calculate penalty term;
16         $Q = Q_1 + Q_2 + Q_3$ by Eqs. (23)-(25)
17   Optimize control action for cost function;
18         $u^* = argmin(Q)$
19   **if** u^* *is feasible* **then**
20   Signal transformation by Eq. (28);
21   Execute;
22   **else**
23   Adjust weighting parameter λ_3;
24   Repeat steps 15-18;
25   **end**
26 **end**

with multiple eloquent constraints, which can be swiftly solved through open source qpOASES.

Remark 2: From Table V, the prediction error of the UAV platform motion grows with the increase of forecast horizon. The correlation between the future motion state and the current state information drops off with the increase of forecast horizon, which would expound this phenomenon. Therefore, the prediction domain of the optimization problem should be set reasonably when considering the prediction error. In this paper, the prediction domain N is defined as 15.

Remark 3: In addition, the continuous velocity signal can be obtained by integrating the control actions u. Therefore, the manipulator joint is always continuous by using (28). It is beneficial for the manipulator on the moving UAV platform to execute millimeter-level active tasks. Then, the control loop is closed by instantiating only the first control value, and periodically reoptimizing the control strategy after updating the state in the next control loop.

Remark 4: In the above multiple constrained predictive optimization problem, although the kinematic feasibility is penalized in (25), it is still possible to generate an infeasible solution. Hence, iterative refinement [56] is leveraged in this work. In each iteration, the optimized solution is checked to improve safety in implementation. If the position of the end-effector is outside the safe boundary, the penalty term weighting parameter λ_3 is increased and solve the optimization problem again.

Remark 5: It should be emphasized that the primary difference between the compensation or attenuation methods and our scheme is the perspective of handling the floating-base disturbance. Different from the previous methods of compensating or suppressing disturbances at the dynamic level, the philosophy of disturbance rejection of the presented scheme is to skillfully utilize the capability of the manipulator to counteract floating-base disturbance. In line with this idea, the UAV fluctuation can be negated by transforming the desired trajectory in $\mathcal{F}_\Delta$ using (9) and (10). Hence, large control magnitude is no longer necessary to achieve the desirable performance.

V. Experiments

A. Baselines and our Method

Two approaches are used for comparison. Each controller is implemented in the aerial manipulator. In [23], the tracking error of the end-effector is directly used as a feedback item (Baseline I). As an improvement, a potential field-based controller is developed in [24] (Baseline II). The details are provided in Appendix. In contrast to the error feedback method, a joint position planner is proposed in Baseline II to handle the floating-base disturbance, where a saturation function and a potential energy function are specified. The primary difference between two baseline methods and our work is the philosophy of addressing the floating-base disturbance. As illustrated in Fig. 5, our work replaces these feedback terms with the predictive optimization scheme. The learning-based approach can rapidly forecast the UAV motion. With the motion prediction as a basis, a control strategy is developed to achieve millimeter-level control accuracy of the end-effector. In addition, for calculating the compensation terms in [23] and [24], the state information of the end-effector should be directly measured by external sensors. In this study, we use forward kinematics to calculate the pose of the end-effector, which reduces the burden of computation. The full algorithmic description is shown in Algorithm 3.

B. Hardware Setup

As shown in Fig. 1, the OptiTrack system is a real-time 6-DOF tracking system with millimeter-level positioning accuracy. Only the position and yaw rotation from the OptiTrack system are applied to control the UAV platform. With respect to the roll and pitch information of the UAV, an inertial measurement unit (IMU9250) built on the STM32F4 MCU is utilized to obtain the attitude data. For obtaining the attitude information in real time, we adopted a complementary filtering algorithm to fuse the data measured by accelerometer and gyroscope, respectively. The motor actuator of the UAV is Sunnysky Eolo 3510 and the manipulator is driven by DYNAMIXEL XM-430 servo actuators with a stall torque of 4.1 N · m. In addition, two voltage regulators are employed to provide a stable voltage for chips. The UAV control algorithm is implemented on-board in the STM32F7 MCU with 100 Hz in the position loop and 500 Hz in the attitude loop. The proposed method runs online on the Manifold-2c

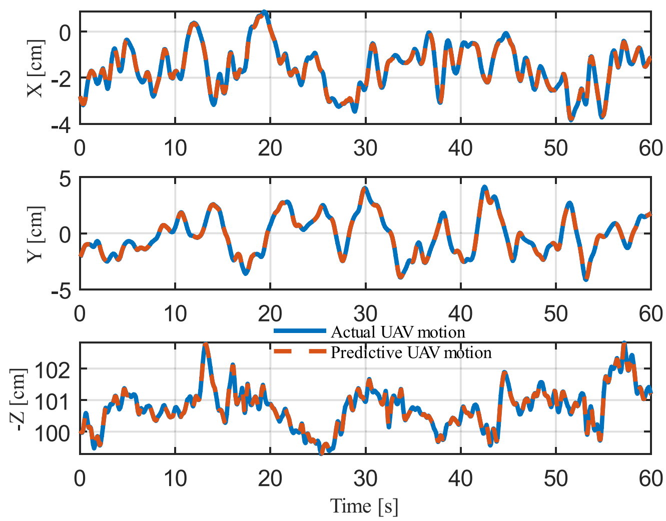

Fig. 6. Online prediction performance of the UAV motion at $i = 10$ ahead in Experiment I (setpoint).

on-board computer with 500 Hz. The control commands are sent to the motor through UART serial port with 4 Mbps baud rate. The Manifold-2c is also employed to establish reliable real-time communication with the ground station through WiFi. Two specific modules are used to receive the end-effector position and manipulator joint measurement information from the ground station and servo actuators, respectively.

C. Evaluation Indices

To quantitatively assess the control performance of the end-effector, three indices (maximum error κ, mean absolute error μ, and standard deviation σ) are defined as

$$\kappa = \max_{1\leq i\leq N}(||P_e^d(i) - P_e(i)||), \mu = \frac{1}{N}\sum_{i=1}^{N}||P_e^d(i) - P_e(i)||$$

$$\sigma = \sqrt{\frac{1}{N-1}\sum_{i=1}^{N}(||P_e^d(i) - P_e(i)|| - \mu)^2}$$

where N is the size of the data set collected during experiments. P_e^d and P_e are defined as the desired and actual trajectories of the end-effector in $\mathcal{F}_I$. The operator $||\cdot||$ denotes the standard Euclidean norm for vectors.

D. Experiment I: Trajectory Tracking Task

During the experiments, the UAV platform is demanded to hover at the given position, while the manipulator is required to track either a setpoint $[0.35, -0.03, 0.76]$ m or a given trajectory. The command trajectory is set as an ellipse shape formulated as $[0.36 + \frac{R\sin(1.5t)}{\sqrt{5/4}}, \frac{R\cos(1.5t)}{\sqrt{5}}, 0.80 - R\cos(1.5t)]$ with $R = 0.06$ m in the task space. Three different controllers are applied for the comparison: Baseline I (feedback-based) versus Baseline II (potential field-based) versus the proposed method.

Fig. 6 depicts the online prediction performance of the UAV motion using learning-based method when the end-effector is required to stay statically in Experiment I. Results illustrate that the motion of the UAV platform can be predicted efficiently and accurately. By virtue of the online prediction information, the UAV platform floating disturbance can be negated by replanning the desired trajectory using (10).

TABLE VI
COMPARISON RESULTS OF THREE CONTROL METHODS (UNIT: cm)

		κ	μ	σ
Experiment I Setpoint	Proposed	**2.08**	**0.70**	**0.36**
	Basseline I	5.33 ↑ 61%	2.82 ↑ 76%	0.90 ↑ 60%
	Baseline II	6.00 ↑ 66%	1.53 ↑ 55%	0.91 ↑ 61%
Experiment I Ellipse	Proposed	**3.74**	**1.10**	**0.88**
	Baseline I	14.03↑ 73%	7.86 ↑ 86%	4.01 ↑ 78%
	Baseline II	11.52↑ 68%	4.10 ↑ 73%	2.46 ↑ 62%
Experiment II Setpoint(Wind)	Proposed	**3.51**	**1.29**	**0.75**
	Baeline I	7.07↑ 51%	2.86 ↑ 55%	1.37 ↑ 46%
	Baseline II	10.72↑ 68%	2.70 ↑ 52%	2.57 ↑ 71%

The tracking performance of the end-effector is illustrated in Fig. 7. The motion ranges of the UAV and the manipulator are represented in the blue and orange shades. Without compensation term in the feedback-based controller, the end-effector cannot guarantee an accurate manipulation. Although the accuracy of the end-effector is improved using Baseline II controller, the presence of the sat function leads to manipulator chattering. It can be intuitively seen that the proposed control scheme has superior performance as displayed in Fig. 7(c). Without loss of generality, the 2-norm of tracking error is selected to draw the error distribution. As illustrated in Fig. 7(d), due to the fact that the prediction information of the UAV platform motion is utilized, the floating-base disturbance is well dissolved. Hence, the proposed predictive optimization scheme can ensure the convergence of tracking error to be a small set.

Subsequently, the test of aerial manipulator tracking a given periodic motion is carried out. For the trajectory tracking case, the UAV platform shows a severe offset of 10 cm near the desired point. The reason is that the coupling disturbances between the manipulator and the UAV become more serious. Fig. 8 depicts the tracking performance comparison of three methods. It is evident that the proposed control scheme can preserve satisfactory tracking performance. These two tests report that the proposed control scheme can effectively ensure the high precision of the end-effector subject to floating-base disturbance. The quantitative results of two tests are listed in Table VI. Bold values represent the best performance metrics.

E. Experiment II: Robustness to Unknown Disturbance

In the second scenario, further verification is conducted to demonstrate the performance of the proposed scheme when unknown external disturbance is injected in the x–y plane. Two 380 W fans are placed at $[0, -1, -1]$ m and $[0, 1, -1]$ m in the inertial reference frame. The maximum wind speed is up to 6 m/s, measured by a digital anemometer AS8556. Meanwhile, the end-effector is expected to hold a desired fix-point under external wind disturbance.

As can be seen in Fig. 9, when a wind disturbance of 6 m/s is involved, the end-effector would present more obvious fluctuations using two baseline approaches. Moreover, Baseline II is

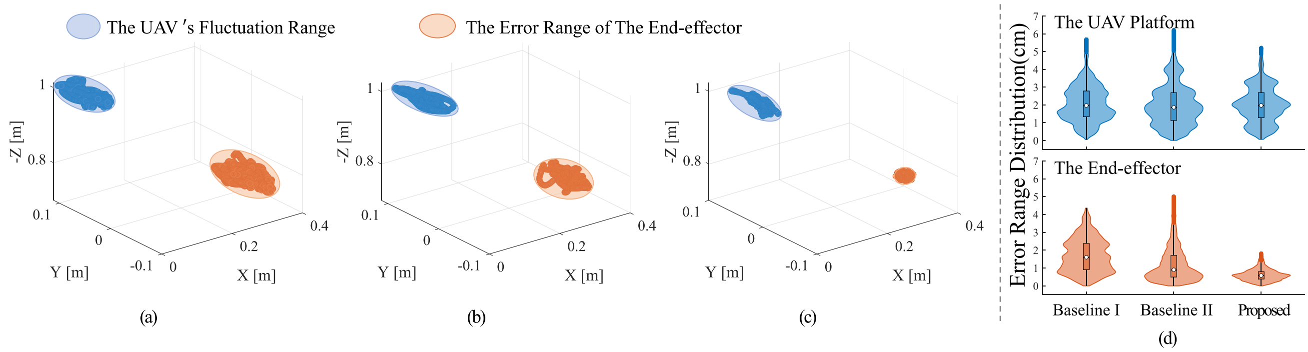

Fig. 7. (a), (b), and (c): Comparative experiments for three control methods of aerial manipulator. The blue and orange shades indicate the range of motion of the UAV and the end-effector. (d) The violin plot shows the tracking error distribution of the UAV platform and the end-effector using three methods.

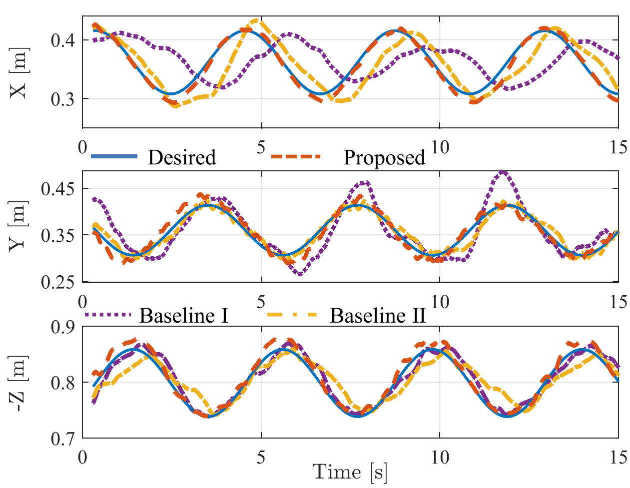

Fig. 8. Tracking performance of aerial manipulator using three methods in Experiment I (Ellipse).

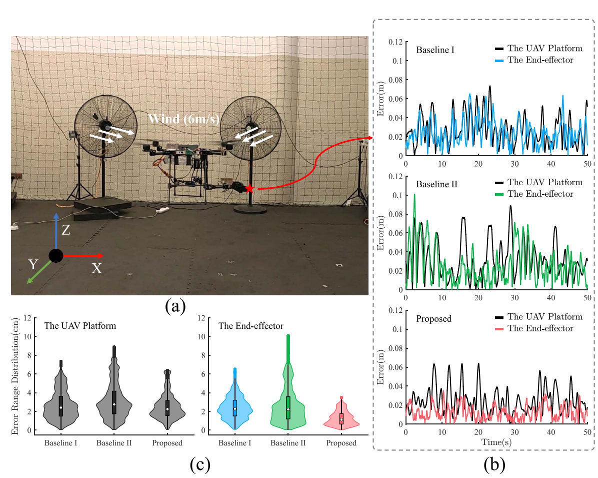

Fig. 9. Flight setup and performance. (a) Experimental scenario that unknown external disturbances are injected in the x-y plane. (b) Depiction of the trajectory tracking performance of three methods. (c) The error distributions of the UAV platform and the end-effector.

especially susceptible to wind disturbance due to the presence of the sat function. Thanks to the deployment of mixing coefficient γ, the further motion of the UAV platform can be well estimated in despite of external wind disturbance. This treatment effectively enhances the manipulation performance. It is emphasized that the steady end-effector also improves the hovering accuracy of the UAV platform, which enables the aerial manipulator to perform high-precision operation tasks.

The improved rates of μ from Baseline I and Baseline II to the proposed scheme are 55% and 52% (from 2.86 cm and 2.70 cm to 1.29 cm). The measures of σ are enhanced by 46% and 71% (from 1.37 cm and 2.57 cm to 0.75 cm). With respect to κ, the proposed scheme attains the superior performance than that of the other methods, with 51% and 68% improvements of the defined metric (from 7.07 cm and 10.72 cm to 3.51 cm). The performance indices highlight that the proposed scheme is applicable for preserving the sound tracking performance even in the case of wind disturbance.

F. Experiment III: Online Learning for Varying Dynamic Process

This scenario is devoted to validating the effectiveness of the proposed method subject to varying nonlinear dynamics. The PID gains of the UAV platform are tuned from the ground station when the system is in flight. Meanwhile, the end-effector is expected to hold a fixed point. As can be observed in Table VII, the uncertainty of the proportion-differentiation (PD) controller gains is set as $\pm30\%$ in the translational loop. For the stability of the aerial manipulator, the uncertainty of the PID controller gains is set as $\pm10\%$ in the rotational loop. Fig. 10 illustrates the experimental procedure. The overall phase is set as: I $\rightarrow$ II $\rightarrow$ III $\rightarrow$ IV $\rightarrow$ III $\rightarrow$ II $\rightarrow$ I $\rightarrow$ V $\rightarrow$ VI $\rightarrow$ VII, while each stage lasts 10 s.

As shown in Fig. 10, with the increase of parameters uncertainties, the UAV platform presents a more violent dynamic process. By incorporating the RLS algorithm, the learning-based scheme achieves superior predictive performance across the whole phase even if the PID gains are changed. It is evident that the learning-based method is well suited to yield stable and accurate motion prediction. The historical states of partial connection weights are depicted in Fig. 11. Therefore, the offline retraining in response to the changing gains can be avoided. Moreover, Table VII depicts the comparison results of the UAV platform and the end-effector. The mean absolute error μ of

TABLE VII
COMPARISON RESULTS OF THE UAV AND THE END-EFFECTOR IN EXPERIMENT III (UNIT: cm)

		κ	μ	σ
Phase I	The UAV	4.83	1.94	0.88
Nominal controller	The end-effector	**1.87**	**0.77**	**0.35**
Phase II	The UAV	5.15	2.17	1.11
$(-10\%, -5\%)$	The end-effector	**2.41**	**0.85**	**0.43**
Phase III	The UAV	4.78	2.59	0.94
$(-20\%, -10\%)$	The end-effector	**2.84**	**1.00**	**0.44**
Phase IV	The UAV	6.28	3.75	1.44
$(-30\%, -10\%)$	The end-effector	**2.25**	**0.92**	**0.46**
Phase V	The UAV	4.78	2.42	0.84
$(+10\%, +5\%)$	The end-effector	**1.86**	**0.93**	**0.41**
Phase VI	The UAV	5.14	2.24	1.23
$(+20\%, +10\%)$	The end-effector	**2.00**	**0.65**	**0.32**
Phase VII	The UAV	5.82	2.04	0.85
$(+30\%, +10\%)$	The end-effector	**1.87**	**0.82**	**0.34**

[1] $(+30\%, +10\%)$ represents $+30\%$ uncertainty in the translational loop and $+10\%$ uncertainty in the rotational loop.

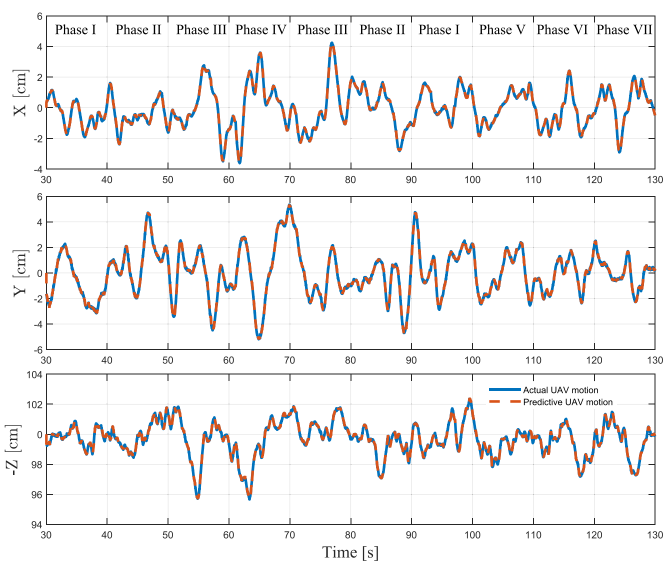

Fig. 10. Online prediction performance of the UAV motion at $i = 10$ ahead when PID gains are tuned.

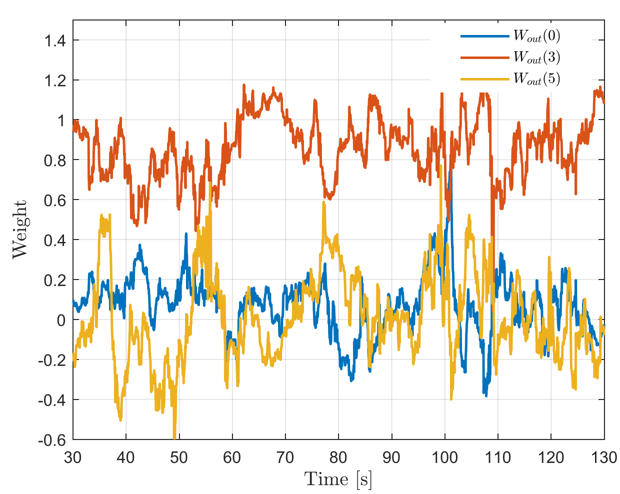

Fig. 11. Historical states of connection weights when PID gains are tuned.

the end-effector is less than 1 cm across the experiment. The performance indices emphasize that the proposed scheme is powerful when the system dynamics is changing. Of course, it is recommended to conduct the retraining process, as the valid initial connection weights can be provided for the online prediction phase.

G. Experiment IV: Millimeter-Level Flying Pick and Peg-in-Hole Task

In an attempt to further explore the capability of the proposed scheme in achieving high precision operation tasks, a challenging pick and peg-in-hole task is designed in this article. The aerial manipulator needs to pick up a pen from the flat base and then precisely insert it into a narrow hole. If the difference in size between the pen and the hole is small, this operation can become very difficult. In this work, the experimental setup of the high-precision operation task employs a pen and a standard hollow cylinder. The hollow cylinder has an inner diameter of 20 mm (see Fig. 1). The diameter of the pen is 11 mm — allowing a play of only ±4.5 mm once the pen is inserted.

This experimental protocol allows for the principled assessment of the ability of aerial manipulator to perform millimeter-level operation tasks. The key snaps together with an experimental video are illustrated in Fig. 12. Hereby our expectations are twofold: 1) the precise position control of the end-effector is demonstrated by picking the pen on top of the bracket; and 2) more interesting and challenging, the ability of performing millimeter-level operations is underlined by placing the pen into the narrow hole. Fig. 13 depicts the trajectory tracking performance of the aerial manipulator during the flying pick and peg-in-hole task. In detail, the end-effector trajectory first follows a desired position to pick the pen. Subsequently, the aerial manipulator tracks a translation along y axis. Finally, the pen is placed into the narrow hole. As shown in partially enlarged views, due to the fact that the prediction information is utilized, satisfactory performance can be achieved at the critical pick and peg-in-hole phase. A set of 15 experiments are conducted, out of which the aerial manipulator successfully completes the task 15 times. It is confirmed that this task would be clearly unfeasible for aerial manipulator, if the floating-base disturbance is not specifically addressed. The ±4.5 mm margin left of the standard hollow cylinder will be completely annihilated by the fluctuation of the UAV platform.

VI. DISCUSSION

A. Control of the UAV Platform

In this article, we pay more attention to maneuvering the manipulator to counteract the floating-base disturbance. Hence, the classical controller previously proposed in [57] is followed. Specifically, in the translational loop, a PD control scheme is applied to track the desired trajectory. In the rotational loop, a PID attitude controller is exploited to ensure the system stability. Without doubt, the control performance of the UAV platform can be improved by adopting advanced controller, such as backstepping control [19] and adaptive control [58].

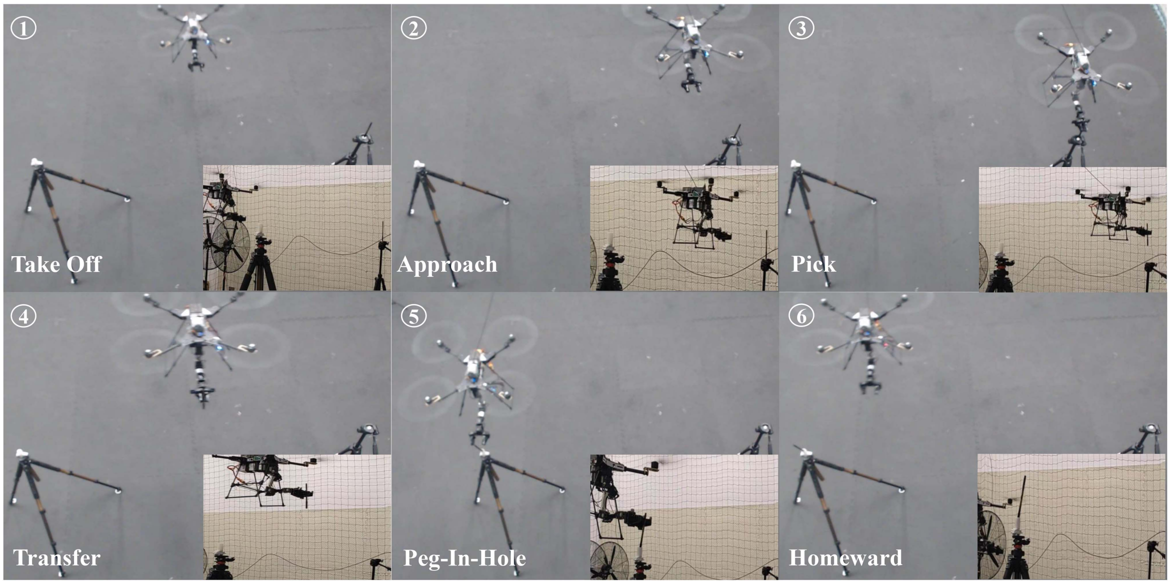

Fig. 12. Key snapshots of the millimeter-level pick and peg-in-hole task. The experimental video can be found online at https://www.youtube.com/playlist?list=PLGsmIGkGCPhKjWKto37d1pl4rayb5ZIX_.

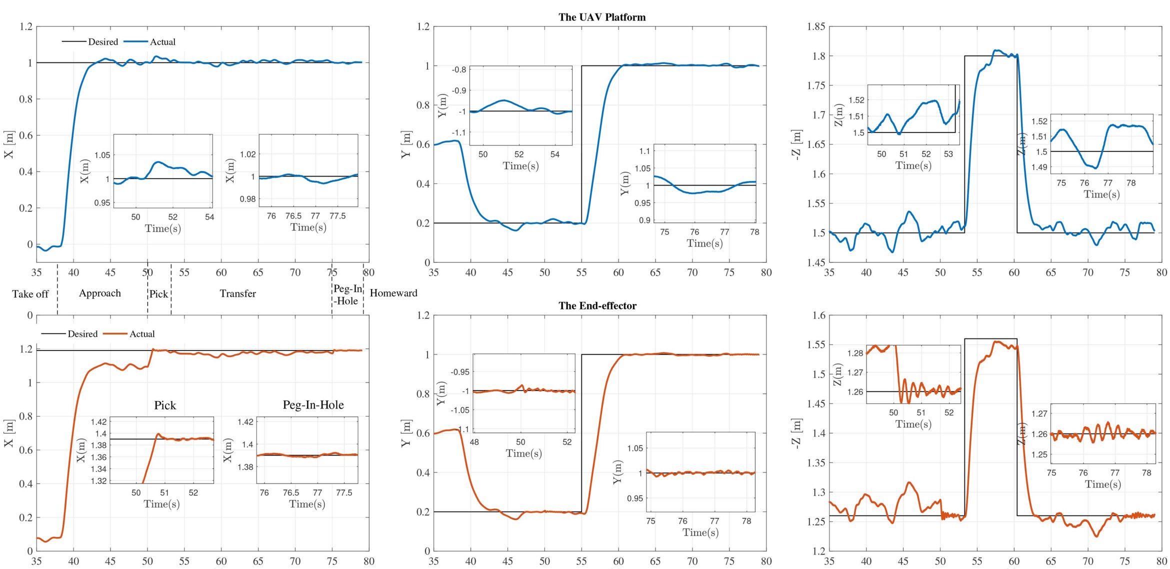

Fig. 13. Trajectory of the aerial manipulator during the flying pick and peg-in-hole task.

Therefore, with respect to the UAV platform, we will also consider designing specific controllers to enhance the control capability in our future work.

B. Selection of the Manipulator Optimization Action

Previous studies of manipulator control formulate the optimization problem in the joint space. However, there exist some disadvantages, if the manipulator joint position is defined as the optimization sequence. On the one hand, (11) shows that the mapping relation from the joint space to the task space is highly nonlinear and nonconvex. Hence, it is very difficult to find the global optimal solution under multiple constraints. In addition, for the manipulator with several DOFs, computing the nonlinear mapping equation across the entire control horizon is also expensive. Hence, this method results in control period of only 20 Hz in [28], which is beyond the requirement of practical application. This control application also serves as a warning that the MPC is not a catchall solution without a reasonable control period. In this article, the acceleration of the end-effector is selected as the control action to enable manipulator to maintain a desired motion under floating-base disturbance. In practice, this method is a convex optimization problem, avoiding a lot of time cost. As a result, computation time is reduced to about 2 ms. Such a high control frequency provides a sound foundation for the achievement of millimeter-level operation tasks.

C. Pick and Peg-in-Hole Task

The flying pick and peg-in-hole task is one of the essential physical interaction tasks in assembly processes of various fields, such as emergency rescue and aerial repair [3], [13]. The ability of achieving millimeter-level operation task by aerial manipulator can significantly expand the field of practical applications.

Peg-in-hole works have been investigated using different methods [11], [13], [25], [59]. In [25], to reduce the coupling effects and enhance the control accuracy of aerial manipulator, the airframe is a hexarotor which weighs 5.5 kg. The control accuracy of the end-effector is held at the centimeter level. A tilt hexarotor with a delta-type manipulator is developed in [11]. The hole has a maximum diameter of 28 mm at the beginning in order to accomplish the challenging task. The dual manipulator structure with active joints and gripper is integrated for achieving the peg-in-hole task in [13] and [59], while the plastic peg is preloaded into the gripper to make sure that the insertion is successful. In addition, additional force sensors are required to measure the contact force. In our study, there is only a margin of ± 4.5 mm in the operation task. To the authors' knowledge, this is the highest accuracy achieved by an aerial manipulator in the flying pick and peg-in-hole task.

VII. Conclusion

In this work, a predictive optimization scheme is presented for aerial manipulator to achieve millimeter-level operation task. The floating-base disturbance is handled by tracking the modified trajectory in $\mathcal{F}_{\Delta}$. Different from the previous studies, a learning-based approach is leveraged to promptly predict the UAV platform motion by incorporating pretrained parameters. Building upon the prediction information, multiple constraints are incorporated in the controller design phase under floating-base disturbance. Finally, we present four scenarios in the domain of precise manipulation that highlight the capabilities of our scheme by comparing other methods. The capacity of the aerial manipulator to perform high-precision operations has been well verified by the millimeter-level flying pick and peg-in-hole task. The achievement of millimeter-level operation accuracy can offer the great potential of aerial manipulator to be applied for more complicated tasks, like restoration of infrastructure facilities.

When extending our method to outdoor scenarios, it may encounter challenges of less high-precision feedback signals of the UAV platform. Fortunately, improvements in either estimation algorithms or in sensors are still potential to obtain accurate state information. Vrba et al.[60] investigated the high-precision flight control with onboard sensors, and impressive performance is demonstrated. For example, laser radar systems can provide a millimeter-level positioning accuracy in long-range. Apart from this, the fusion of camera and inertial measurement unit has great potential to achieve high-precision positioning. These approaches may be extended to our next generation of the aerial manipulator in the future.

Appendix

As a performance measure, two baseline methods are compared.

1) *Baseline I:* A classical feedback-based controller is compared. The controller of the manipulator is defined

$$\dot{q}_{\mathrm{re}} = \boldsymbol{T}_2^{\dagger}\dot{P}_e^d - \beta\boldsymbol{T}_2^{\top}\Delta P_e \tag{31}$$

where $\dot{q}_{\mathrm{re}}$ is employed as input to the manipulator dynamic controller. $\dot{P}_e^d$ is the desired velocity of the end-effector in $\mathcal{F}_I$. ΔP_e is defined as the tracking error in $\mathcal{F}_I$. $\boldsymbol{T}_2$ represents the mapping matrix from the manipulator joint space to the inertial reference frame $\mathcal{F}_I$. β denotes the positive gain. The error feedback term is employed to suppress the floating-base disturbance.

2) *Baseline II:* As an improvement to Baseline I, a potential field-based controller is developed

$$\dot{q}_{\mathrm{re}} = \boldsymbol{T}_2^{\dagger}\dot{P}_e^d - \alpha\boldsymbol{T}_2^{\top}\Delta\varepsilon - k\boldsymbol{T}_2^{\dagger}\mathrm{sat}(a\Delta P_e) \tag{32}$$

where α and k denote the positive gains. a is a positive parameter. The last term is added to directly compensate the floating-base disturbance. The gradient function $\Delta\varepsilon$ is defined as

$$\Pi(\Delta P_e) = K_p[\max(0, ||\Delta P_e||^2 - \zeta)]^L$$
$$\Delta\varepsilon = \frac{\partial\Pi(\Delta P_e)}{\partial\Delta P_e}, 3 \leq L \tag{33}$$

where K_p and ζ are the designed energy constants.

References

[1] D. Mellinger, Q. Lindsey, M. Shomin, and V. Kumar, “Design, modeling, estimation and control for aerial grasping and manipulation,” in *Proc. IEEE/RSJ Int. Conf. Intell. Robots Syst.*, 2011, pp. 2668–2673.

[2] H. Bonyan Khamseh, F. Janabi-Sharifi, and A. Abdessameud, “Aerial manipulation–A literature survey,” *Robot. Auton. Syst.*, vol. 107, pp. 221–235, 2018.

[3] A. Ollero, M. Tognon, and A. Suarez, “Past, present, and future of aerial robotic manipulators,” *IEEE Trans. Robot.*, vol. 38, no. 1, pp. 626–645, Feb. 2022.

[4] K. Zhang et al., “Aerial additive manufacturing with multiple autonomous robots,” *Nature*, vol. 609, pp. 709–717, 2022.

[5] P. Chermprayong, K. Zhang, F. Xiao, and M. Kovac, “An integrated delta manipulator for aerial repair: A new aerial robotic system,” *IEEE Robot. Automat. Mag.*, vol. 26, no. 1, pp. 54–66, Mar. 2019.

[6] G. B. Haberfeld, D. Sun, and N. Hovakimyan, “Stabilization and optimal trajectory generation for a compact aerial manipulation system with a delta-type parallel robot,” in *Proc. Int. Conf. Unmanned Aircr. Syst.*, 2018, pp. 1091–1100.

[7] E. Cuniato et al., “Design and control of a micro overactuated aerial robot with an origami delta manipulator,” in *Proc. IEEE Int. Conf. Robot. Automat.*, 2023, pp. 5352–5358.

[8] R. Rashad et al., “Energy aware impedance control of a flying end-effector in the port-Hamiltonian framework,” *IEEE Trans. Robot.*, vol. 38, no. 6, pp. 3936–3955, Dec. 2022.

[9] K. Bodie et al., “Active interaction force control for contact-based inspection with a fully actuated aerial vehicle,” *IEEE Trans. Robot.*, vol. 37, no. 3, pp. 709–722, Jun. 2021.

[10] K. Bodie, M. Tognon, and R. Siegwart, “Dynamic end effector tracking with an omnidirectional parallel aerial manipulator,” *IEEE Robot. Automat. Lett.*, vol. 6, no. 4, pp. 8165–8172, Oct. 2021.

[11] M. Ryll et al., “6D interaction control with aerial robots: The flying end-effector paradigm,” *Int. J. Robot. Res.*, vol. 38, pp. 1045–1062, 2019.

[12] V. Lippiello, G. A. Fontanelli, and F. Ruggiero, “Image-based visual-impedance control of a dual-arm aerial manipulator,” *IEEE Robot. Automat. Lett.*, vol. 3, no. 3, pp. 1856–1863, Jul. 2018.

[13] M. Orsag, C. Korpela, S. Bogdan, and P. Oh, "Dexterous aerial robots–mobile manipulation using unmanned aerial systems," *IEEE Trans. Robot.*, vol. 33, no. 6, pp. 1453–1466, Dec. 2017.
[14] M. Jafarinasab, S. Sirouspour, and E. Dyer, "Model-based motion control of a robotic manipulator with a flying multirotor base," *IEEE/ASME Trans. Mechatron.*, vol. 24, no. 5, pp. 2328–2340, Oct. 2019.
[15] G. Zhang, Y. He, B. Dai, F. Gu, J. Han, and G. Liu, "Robust control of an aerial manipulator based on a variable inertia parameters model," *IEEE Trans. Ind. Electron.*, vol. 67, no. 11, pp. 9515–9525, Nov. 2020.
[16] Y.-C. Liu and C.-Y. Huang, "DDPG-based adaptive robust tracking control for aerial manipulators with decoupling approach," *IEEE Trans. Cybern.*, vol. 52, no. 8, pp. 8258–8271, Aug. 2022.
[17] S. Kim, H. Seo, S. Choi, and H. J. Kim, "Vision-guided aerial manipulation using a multirotor with a robotic arm," *IEEE/ASME Trans. Mechatron.*, vol. 21, no. 4, pp. 1912–1923, Aug. 2016.
[18] D. Lee, H. Seo, I. Jang, S. J. Lee, and H. J. Kim, "Aerial manipulator pushing a movable structure using a DOB-based robust controller," *IEEE Robot. Automat. Lett.*, vol. 6, no. 2, pp. 723–730, Apr. 2021.
[19] S. Kim, S. Choi, H. Kim, J. Shin, H. Shim, and H. J. Kim, "Robust control of an equipment-added multirotor using disturbance observer," *IEEE Trans. Control Syst. Technol.*, vol. 26, no. 4, pp. 1524–1531, Jul. 2018.
[20] H. Cao, Y. Li, C. Liu, and S. Zhao, "ESO-based robust and high-precision tracking control for aerial manipulation," *IEEE Trans. Automat. Sci. Eng.*, to be published, doi: 10.1109/TASE.2023.3260874.
[21] S. A. Emami and A. Banazadeh, "Simultaneous trajectory tracking and aerial manipulation using a multi-stage model predictive control," *Aerosp. Sci. Technol.*, vol. 112, 2021, Art. no. 106573.
[22] H. Cao, Y. Wu, and L. Wang, "Adaptive NN motion control and predictive coordinate planning for aerial manipulators," *Aerosp. Sci. Technol.*, vol. 126, 2022, Art. no. 107607.
[23] K. Lynch and F. C. Park, *Modern Robotics: Mechanics, Planning, and Control*. Cambridge, U.K.: Cambridge Univ. Press, 2017.
[24] S. Lyu and C. C. Cheah, "Human–robot interaction control based on a general energy shaping method," *IEEE Trans. Control Syst. Technol.*, vol. 28, no. 6, pp. 2445–2460, Nov. 2020.
[25] W. Dong, Z. Ma, X. Sheng, and X. Zhu, "Centimeter-level aerial assembly achieved with manipulating condition inference and compliance," *IEEE/ASME Trans. Mechatronics*, vol. 27, no. 3, pp. 1660–1671, Jun. 2022.
[26] J. Woolfrey, W. Lu, and D. Liu, "Predictive end-effector control of manipulators on moving platforms under disturbance," *IEEE Trans. Robot.*, vol. 37, no. 6, pp. 2210–2217, Dec. 2021.
[27] K.-D. Nguyen and H. Dankowicz, "Adaptive control of underactuated robots with unmodeled dynamics," *Robot. Auton. Syst.*, vol. 64, pp. 84–99, 2015.
[28] J. Woolfrey, D. Liu, and M. Carmichael, "Kinematic control of an autonomous underwater vehicle-manipulator system (AUVMS) using autoregressive prediction of vehicle motion and model predictive control," in *Proc. IEEE Int. Conf. Robot. Automat.*, 2016, pp. 4591–4596.
[29] L. Marković, M. Car, M. Orsag, and S. Bogdan, "Adaptive stiffness estimation impedance control for achieving sustained contact in aerial manipulation," in *Proc. IEEE Int. Conf. Robot. Automat.*, 2021, pp. 117–123.
[30] Y. Chen, J. Liang, Y. Wu, Z. Miao, H. Zhang, and Y. Wang, "Adaptive sliding-mode disturbance observer-based finite-time control for unmanned aerial manipulator with prescribed performance," *IEEE Trans. Cybern.*, vol. 53, no. 5, pp. 3263–3276, May 2023.
[31] E. Tal and S. Karaman, "Accurate tracking of aggressive quadrotor trajectories using incremental nonlinear dynamic inversion and differential flatness," *IEEE Trans. Control Syst. Technol.*, vol. 29, no. 3, pp. 1203–1218, May 2021.
[32] G. Ciattaglia, G. Iadarola, L. Senigagliesi, S. Spinsante, and E. Gambi, "UAV propeller rotational speed measurement through FMCW radars," *Remote Sens.*, vol. 15, no. 1, pp. 1–20, 2023.
[33] A. Suarez, A. E. Jimenez-Cano, V. M. Vega, G. Heredia, A. Rodriguez-Castaño, and A. Ollero, "Design of a lightweight dual arm system for aerial manipulation," *Mechatronics*, vol. 50, pp. 30–44, 2018.
[34] B. Siciliano, L. Sciavicco, L. Villani, and G. Oriolo, *Robotics: Modelling, Planning and Control*. New York, NY, USA: Springer, 2010.
[35] T. Sun, B. Lian, S. Yang, and Y. Song, "Kinematic calibration of serial and parallel robots based on finite and instantaneous screw theory," *IEEE Trans. Robot.*, vol. 36, no. 3, pp. 816–834, Jun. 2020.
[36] T. Justin, L. Giuseppe, P. Joseph, S. Koushil, and V. Kumar, "Toward autonomous avian-inspired grasping for micro aerial vehicles," *Bioinspiration Biomimetics.*, vol. 9, no. 2, 2014, Art. no. 025010.
[37] D. Mellinger, M. Shomin, N. Michael, and V. Kumar, "Cooperative grasping and transport using multiple quadrotors," *Distrib. Auton. Robot. Syst.*, vol. 83, pp. 545–558, 2013.
[38] S. H. Patel and T. M. Sobh, "Manipulator performance measures - a comprehensive literature survey," *J. Intell. Robot. Syst.*, vol. 77, pp. 547–570, 2015.
[39] D. E. Whitney, "Resolved motion rate control of manipulators and human prostheses," *IEEE Trans. Man- Mach. Syst.*, vol. 10, no. 2, pp. 47–53, Jun. 1969.
[40] R. Krishan, D. Vibhavari, H. Jesse, T. Ben, M. Michael, and S. Niko, "Bayesian controller fusion: Leveraging control priors in deep reinforcement learning for robotics," *Int. J. Robot. Res.*, vol. 42, no. 3, pp. 123–146, 2023, doi: 10.1177/02783649231167210.
[41] S. Kim, S. Choi, and H. J. Kim, "Aerial manipulation using a quadrotor with a two DOF robotic arm," in *Proc. IEEE/RSJ Int. Conf. Intell. Robots Syst.*, 2013, pp. 4990–4995.
[42] A. A. Shabana, *Dynamics of Multibody Systems*. Cambridge, U.K.: Cambridge Univ. Press, 2020.
[43] G. V. Raffo, M. G. Ortega, and F. R. Rubio, "An integral predictive/nonlinear H∞ control structure for a quadrotor helicopter," *Automatica*, vol. 46, no. 1, pp. 29–39, 2010.
[44] C. Gaz, M. Cognetti, A. Oliva, P. Robuffo Giordano, and A. De Luca, "Dynamic identification of the Franka Emika panda robot with retrieval of feasible parameters using penalty-based optimization," *IEEE Robot. Automat. Lett.*, vol. 4, no. 4, pp. 4147–4154, Oct. 2019.
[45] Y. Huang, J. Ke, X. Zhang, and J. Ota, "Dynamic parameter identification of serial robots using a hybrid approach," *IEEE Trans. Robot.*, vol. 39, no. 2, pp. 1607–1621, Apr. 2023.
[46] L. Guo and W. H. Chen, "Disturbance attenuation and rejection for systems with nonlinearity via DOBC approach," *Int. J. Robust Nonlinear Control*, vol. 15, no. 3, pp. 109–125, 2005.
[47] M. Bowthorpe and M. Tavakoli, "Generalized predictive control of a surgical robot for beating-heart surgery under delayed and slowly-sampled ultrasound image data," *IEEE Robot. Automat. Lett.*, vol. 1, no. 2, pp. 892–899, Jul. 2016.
[48] S. Roberts, M. Osborne, M. Ebden, N. G. S. Reece, and S. Aigrain, "Gaussian processes for time-series modelling," *Roy. Soc. A, Math., Phys. Eng. Sci.*, vol. 371, no. 1984, pp. 892–899, 2013.
[49] H. Jaeger and H. Haas, "Harnessing nonlinearity: Predicting chaotic systems and saving energy in wireless communication," *Science*, vol. 304, no. 5667, pp. 78–80, 2004.
[50] J. P. Jordanou, E. A. Antonelo, and E. Camponogara, "Echo state networks for practical nonlinear model predictive control of unknown dynamic systems," *IEEE Trans. Neural Netw. Learn. Syst.*, vol. 33, no. 6, pp. 2615–2629, Jun. 2022.
[51] D. Sussillo and L. Abbott, "Generating coherent patterns of activity from chaotic neural networks," *Neuron*, vol. 63, no. 4, pp. 544–557, 2009.
[52] J. Swevers, C. Ganseman, D. Tukel, J. de Schutter, and H. Van Brussel, "Optimal robot excitation and identification," *IEEE Trans. Robot. Automat.*, vol. 13, no. 5, pp. 730–740, Oct. 1997.
[53] L. Hewing, J. Kabzan, and M. N. Zeilinger, "Cautious model predictive control using Gaussian process regression," *IEEE Trans. Control Syst. Technol.*, vol. 28, no. 6, pp. 2736–2743, Nov. 2020.
[54] S. Kim, A. Shukla, and A. Billard, "Catching objects in flight," *IEEE Trans. Robot.*, vol. 30, no. 5, pp. 1049–1065, Oct. 2014.
[55] Z. T. Dydek, A. M. Annaswamy, and E. Lavretsky, "Adaptive control of quadrotor UAVs: A design trade study with flight evaluations," *IEEE Trans. Control Syst. Technol.*, vol. 21, no. 4, pp. 1400–1406, Jul. 2013.
[56] F. Gao, L. Wang, B. Zhou, X. Zhou, J. Pan, and S. Shen, "Teach-repeat-replan: A complete and robust system for aggressive flight in complex environments," *IEEE Trans. Robot.*, vol. 36, no. 5, pp. 1526–1545, Oct. 2020.
[57] W. Zhang et al., "Design of an aerial manipulator system applied to capture missions," in *Proc. Int. Conf. Unmanned Aircr. Syst.*, 2021, pp. 1063–1069.
[58] G. Antonelli, E. Cataldi, F. Arrichiello, P. Robuffo Giordano, S. Chiaverini, and A. Franchi, "Adaptive trajectory tracking for quadrotor mavs in presence of parameter uncertainties and external disturbances," *IEEE Trans. Control Syst. Technol.*, vol. 26, no. 1, pp. 248–254, Jan. 2018.
[59] M. Car, A. Ivanovic, M. Orsag, and S. Bogdan, "Impedance based force control for aerial robot peg-in-hole insertion tasks," in *Proc. IEEE/RSJ Int. Conf. Intell. Robots Syst.*, 2018, pp. 6734–6739.
[60] M. Vrba et al., "Autonomous capture of agile flying objects using UAVs: The MBZIRC 2020 challenge," *Robot. Auton. Syst.*, vol. 149, 2022, Art. no. 103970.

Meng Wang received the B.S. degree in automation science and engineering from Northwestern Polytechnical University, Xi'an, China, in 2020. He is currently working toward the Ph.D. degree in control theory and control engineering with the School of Automation Science and Electrical Engineering, Beihang University, Beijing, China.

His current research interests include adaptive control, aerial manipulator, and intelligent control of robotic systems.

Zeshuai Chenreceived the B.S. degree in aircraft control and information engineering from Northwestern Polytechnical University, Xi'an, China, in 2020. He is currently working toward the Ph.D. degree in control theory and control engineering with the School of Automation Science and Electrical Engineering, Beihang University, Beijing, China.

His current research interests include aerial manipulator and control of robotic systems.

Kexin Guo received the B.S. degree in control theory and control engineering from Beijing Institute of Technology, Beijing, China, in 2011, the M.S. degree in instrumentation science and technology from Beihang University, Beijing, China, in 2014, and the Ph.D. degree in electrical and electronic engineering from Nanyang Technological University, Singapore, in 2018.

He was a Post-Doctoral Fellow of the "Zhuoyue" program with the School of Automation Science and Electrical Engineering, Beihang University, in 2019. Since 2021, he has been an Associate Professor with the School of Aeronautic Science and Engineering, Beihang University, Beijing, China. His current research interests include GNSS-denied localization, bio-inspired control and safety control of unmanned aerial vehicles.

Dr. Guo was a recipient of the Best Paper and Best Paper Finalist at international conferences.

Xiang Yu received the B.S., M.S., and Ph.D. degrees in automation science and engineering from Northwestern Polytechnical University, Xi'an, China, in 2003, 2004, and 2008, respectively.

He is currently a Professor with the School of Automation Science and Electrical Engineering, Beihang University, Beijing, China. He was a Post-Doctoral Research Fellow with the Department of Electrical and Computer Engineering, Western University, London, ON, Canada, and a Research Associate with the Department of Mechanical, Industrial and Aerospace Engineering, Concordia University, Montreal, QC, Canada. He has authored more than 70 prestigious journal papers and a monograph, including IEEE TRANSACTIONS, *AIAA Journals*, and *Progress in Aerospace Sciences*. His current research interests include safety control of unmanned aerial vehicles, autonomous navigation and control of hypersonic vehicles.

Dr. Yu was a recipient of the Recruitment Program for Young Professionals, First Prize of Science and Technology Progress Award of China Instrument and Control Society, Youth Science and Technology Award of Chinese Society of Aeronautics and Astronautics, the Best Paper and Best Paper Finalist at international conferences. He has also served as the Associate Editors of *Journal of Field Robotics, Journal of Intelligent & Robotic Systems, Asian Journal of Control, and Chinese Journal of Aeronautics*, Program Co-Chair, Invitation Chair, and IPC Member of several academic conferences.

Youmin Zhang (Fellow, IEEE) (Fellow, IEEE) received the B.S., M.S., and Ph.D. degrees in automatic control from the Department of Automatic Control, Northwestern Polytechnical University, Xi.an, China, in 1983, 1986, and 1995, respectively. He is currently a Professor with the Department of Mechanical, Industrial and Aerospace Engineering, Concordia University, Montreal, QC, Canada. He has authored or coauthored eight books, more than 600 journal and conference papers. His research interests include the areas of monitoring, diagnosis and physical fault/cyber-attack tolerant/resilient control, guidance, navigation and control of unmanned systems and smart grids, with applications to forest fires and smart cities in the framework of cyber-physical systems by combining with remote sensing techniques.

Dr. Zhang is a Fellow of CSME, a Senior Member of AIAA, President of International Society of Intelligent Unmanned Systems (ISIUS) during 2019–2022, and a technical committee member of several scientific societies. He has been the Editor-in-Chief (EIC), Editorial Advisory Board Member of several journals, including as a Member of Board Member of Governors and Representatives for *Journal of Intelligent and Robotic Systems*, an Associate Editor for IEEE TRANSACTIONS ON INDUSTRIAL ELECTRONICS, IEEE TRANSACTIONS ON NEURAL NETWORKS AND LEARING SYSTEMS, IEEE TRANSACTION ON CIRCUITS AND SYSTEMS–II: EXPRESS BRIEFS, IET *Cyber-systems and Robotics, Unmanned Systems, Security and Safety*, and the Deputy EIC of *Guidance, Navigation and Control*.

Lei Guo (Fellow, IEEE) was born in Qufu, China, in 1966. He received the B.S. degree in fundamental mathematics and the M.S. degree in operational research and cybernetics from Qufu Normal University, Qufu, China, in 1988 and 1991, respectively, and the Ph.D. degree in control engineering from Southeast University, Nanjing, China, in 1997.

From 1991 to 1994, he was a Lecturer with Qingdao University, Qingdao, China. From 1997 to 1999, he was a Postdoctoral Fellow with Southeast University. From 1999 to 2000, he was a Research Fellow with IRCCyN, Nantes, Frances. From 2000 to 2003, he was a Research Fellow with the University of Glasgow, Glasgow, U.K., Loughborough University, Loughborough, U.K., and the University of Manchester Institute of Science and Technology, Manchester, U.K. In 2004, he joined the Institute of Automation, Southeast University, as a Professor. In 2006, he became a Professor with the School of Instrumentation and Opto-Electronics Engineering, Beihang University, Beijing, China, where he is currently with the School of Automation Science and Electronic Engineering. He is also an Academician of the Chinese Academy of Sciences and a Changjiang Distinguished Professor of the Ministry of Education of China. He has authored or coauthored more than 420 papers and six academic books, and more than 120 invention patents. His research interests include anti-disturbance control theory and applications.

Dr. Guo was the recipient of the National Nature Science Awards, National Technology Invention Awards, National Pioneer Innovation Award, Awardee of the National Science Fund for Distinguished Young Scholars of China, and more than five provincial and ministerial level science and technology awards. He was an Editor for five journals.

Wei Wang received the B.S. and M.S. degrees in automatic control from Beihang University, Beijing, China, in 1988 and 1991, respectively, and the Ph.D. degree in control theory and control engineering from the China Academy of Launch Vehicle Technology, Beijing, in 1998.

He is currently an Academician of the Chinese Academy of Sciences, Academician of the International Academy of Astronautics. He was granted more than 40 invention patents and authored or coauthored five academic books. His current research interests include new inertial devices, spacecraft guidance control, high-precision navigation systems, and GNC microsystems.

Dr. Wang was the recipient of the two National Technology Invention Awards, two National Science and Technology Progress Awards, eight provincial and ministerial level science and technology awards. He is also the Chief Editor of *Advanced Devices and Instrumentation*.